INFORMATION TO USERS

This manuscript has been reproduced from the microfilm master. UMI films the text directly from the original or copy submitted. Thus, some thesis and dissertation copies are in typewriter face, while others may be from any type of computer printer.

The quality of this reproduction is dependent upon the quality of the copy submitted. Broken or indistinct print, colored or poor quality illustrations and photographs, print bleedthrough, substandard margins, and improper alignment can adversely affect reproduction.

In the unlikely event that the author did not send UMI a complete manuscript and there are missing pages, these will be noted. Also, if unauthorized copyright material had to be removed, a note will indicate the deletion.

Oversize materials (e.g., maps, drawings, charts) are reproduced by sectioning the original, beginning at the upper left-hand corner and continuing from left to right in equal sections with small overlaps.

ProQuest Information and Learning
300 North Zeeb Road, Ann Arbor, MI 48106-1346 USA
800-521-0600

UMI®

UNIVERSITY of CALIFORNIA
Santa Barbara

A Terahertz Detector Based on Intersubband Transitions in Quantum Wells

A dissertation submitted in partial satisfaction of the
requirements for the degree of

Doctor of Philosophy

in

Physics

by

Carey Cates

Committee in charge:

Professor Mark Sherwin, Chair
Professor Philip Lubin
Professor Andreas Ludwig

September 2002

UMI Number: 3064705

Copyright 2002 by
Cates, Carey Lynn

All rights reserved.

UMI®

UMI Microform 3064705
Copyright 2002 by ProQuest Information and Learning Company.
All rights reserved. This microform edition is protected against
unauthorized copying under Title 17, United States Code.

ProQuest Information and Learning Company
300 North Zeeb Road
P.O. Box 1346
Ann Arbor, MI 48106-1346

The dissertation of Carey Lynn Cates is approved.

Philip Lubin

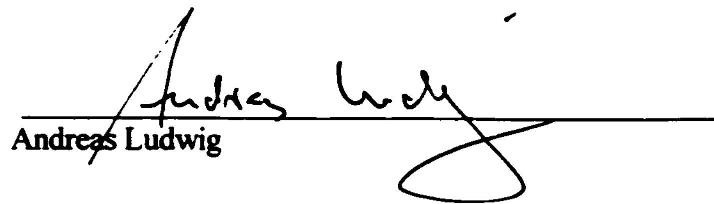

Andreas Ludwig

Mark Sherwin, Committee Chair

July 2002

A Terahertz Detector Based on Intersubband Transitions in Quantum Wells

Copyright 2002

by

Carey Cates

Acknowledgements

This dissertation comes at the end of a long road, and I thank everyone who has helped me along the way. I particularly wish to thank my advisor, Mark Sherwin, for his patience with this project and with me, even after the long periods when nothing worked. I also with to thank him for giving me the time and freedom to learn about what interests me, whether it be cleanroom processing or business courses, and for letting me go away for an internship. Not many advisors are as supportive in this respect and I truly appreciate it. I have also had the good fortune to work with a lo t of great people in and around the Free Electron Lasers labs. Thanks to you all, for your friendship and making the lab a fun place to work, as well as for helping me learn a lot of experimental technique.

Special mention must be made of a number of people without whom I never would have gotten my project to work. Bob Hill, Neil Baker, Brian Thibeault, and Jack Whaley kept the cleanroom up and running (no mean feat!) and graciously helped me whenever something went haywire. Dave Enyeart (I feel I still owe you cheesecake for your patient FEL tuning help) Dean White, and Jerry Ramian were essential to having sources with which to test my detectors. The friendly and super-capable staff of the machine shops always good-naturedly helped me with the random pieces and parts I needed, and helped improve the designs as well. Thanks also go to the many people of the staffs of the Quantum Institute, QUEST, and IQUEST, without whom I could not have purchased anything, travelled anywhere, gotten paid, and so much more. Even if (most of) you have never been in the cleanroom or the other labs, your efforts are evident in every part of this research. Thank you to Rick Lytel and Howard Davidson for giving me the chance to join their group of RASCALs for a summer internship at Sun Microsystems Labs in Mountain View. I really don't know if I would have ever graduated without that wonderful opportunity to have fun with science and business. Thank you to John Kolena, who started my journey in Physics, and to Hadi Ghaemi and Bennett Goldberg who first let me

have fun in experiments (and crash their computers on a regular basis). To Frank Hegmann, Keith Craig, Gabriel Briceño, and Jon Williams, that I worked with directly with, thanks for sharing your insight and experience with me. To Brendan and Yuvaraj, who will continue this project beyond what I have done, the best of luck to you, and always feel free to ask me questions! The many others in the Sherwin group who came before me and after me also helped me learn a lot, both by my aswering my questions, and asking by me theirs. Best wishes to you all.

Above all, I cannot thank enough my family and my friends, without whom I never would have survived. You have really helped me when I needed it most, offering support and encouragement, helping me deal with late nights in the cleanroom and FEL, lending me good escapist fiction, and so on. I owe you my sanity and the last shreds of my sense of humor. My heartfelt thanks go to you all.

Curriculum Vitæ

Carey Cates

Personal

Birthdate	December 19, 1972, Washington, D.C., United States of America

Education

September 2002	Ph.D. in Physics, Univeristy of California Santa Barbara.
December 2000	Certificate in Graduate Program in Management Practice, University of California Santa Barbara.
December 1997	M.A. in Physics, University of California Santa Barbara.
May 1994	B.A. in Physics, Summa Cum Laude, Boston University.
June 1990	Diploma, North Carolina School for Science and Mathematics.

Employment

1995-2002	Graduate Student Researcher, Physics Department and Center for Terahertz Science and Technology, University of California Santa Barbara, Santa Barbara, CA. Advisor: Mark S. Sherwin.
2000	Graduate Student Intern, Sun Microsystems Laboratories, Mountain View, CA. Supervisor: Rick Lytel.

1994-1995	National Physical Sciences Consortium Fellow and Intern. NASA Marshall Space Flight Center, Huntsville, AL. Supervisors: Henry Waites and Jon Rakoczy.
1992-1994	Undergraduate Research Assistant. Physics Department, Boston University, Boston, MA. Advisor: Bennett B Goldberg.
1991.1992	Co-op Pre-professional Engineer. IBM Corporation, Raleigh, NC. Supervisor: Joe Lamoreux.

Awards and Honors

1994-2000	National Physical Sciences Consortium Fellow.
1990-1994	Boston University Trustee Scholar.
1990-1994	IBM Thomas J. Watson Sr. Memorial Scholarship.

Publications

1. "Detection of Terahertz Light with Intersubband Transitions in Semiconductor Quantum Wells". Proceedings of the Far-IR, Sub-mm & MM Detector Technology Workshop, April 1-3, 2002, Monterey, CA, in publication.
2. "Tunable Antenna-Coupled Intersubband Terahertz (TACIT) Detectors for Operation Above 4K". Proceedings of the Eleventh International Symposium on Sapce Terahertz Technology, May 1-3, 2000, Ann Arbor, MI, pp. 389-96, 2000.
3. "Quantum Well Based Tunable Antenna-Coupled Intersubband Terahertz (TACIT) Detectors at 1.8-2.4 THz". Proceedings of SPIE - the International Society for Optical Engineering, vol. 3617, pp.58-66, San Jose, CA, January 1999.

4. "A Non-bolometric Model for a Tunable Antenna-Coupled Intersubband Terahertz (TACIT) Detector", Proceedings of the Ninth International Symposium on Sapce Terahertz Technology, March 17-19, 1998, Pasadena, CA, pp. 597-606, 1998.

5. "A Concept for a Tunable Antenna-Coupled Intersubband Terahertz (TACIT) Detector", Physica E, vol.2, no.1-4, pp.463-7, Netherlands, 15 July 1998.

6. "Low Temperature Near Field Spectroscopy and Microscopy", Ultramicroscopy, vol.57, no.2-3, pp.165-8, Netherlands, Feb. 1995.

Abstract

A Terahertz Detector Based on Intersubband Transitions in Quantum Wells

by

Carey Cates

A new kind of far infrared detector based on intersubband transitions in semiconductor quantum wells has been made. Detection in both in-plane photoconductive and gate photovoltage modes has been demonstrated in two different quantum well structures at temperatures well above 4K. These mechanisms may allow future iterations of these detectors to fly on satelites without the complication, weight, and cost of liquid cryogens. In photoconductive detection, electrons absorb Terahertz light in intersubband transitions, raising the electron temperature. This change is registered, through the temperature-dependent electron mobility, as a change in the in-plane resistance of the device. Photoconductive detection was observed for a double quantum well structure at temperatures from 5K to over 75K, peaking at 20K. The temperature dependence is in good qualitative agreement with a bolometric model. In gate photovoltage detection, Terahertz light raises electrons from the ground to the excited subband, displacing the electron gas from its unilluminated equilibrium position. This net displacement changes the capacitance between the front gate metalization and the sheet of charge in the quantum well. Also, the rise in electron temperature causes a change in the chemical potential. Both effects contribute to the gate photovoltage. A combined circuit model with a single relaxation time explains features of the data that cannot be explained by either effect alone. Using this circuit model, the relaxation time has been extracted from simultaneous gate photovoltage and absorption measurements on a single wide quantum well with the charge density and electric field varied independently. Two issues limit the application of this model, however. The model nonlinear equation diverges without a

solution at low charge densities, and the calculated electron temperatures are unreasonably large. The model equation solutions match the data by the small difference of two larger terms. The mathematical non-robustness of this situation may make the model sensitive to small changes in the input parameters, possibly even to within the experimental error of the parameters. Nonetheless, these measurements indicate that both the polarization and chemcial potential effects should be considered for future quantum well gate photovoltage devices and for engineering the thermal design of future Terahertz detectors.

Contents

List of Figures xiii

List of Tables xv

1 Introduction 1

2 Background 3
- 2.1 THz Technology 3
- 2.2 THz Detectors 4
- 2.3 Survey of THz Detector Types 6
  - 2.3.1 Superconductors 6
  - 2.3.2 Pyroelectric Materials 10
  - 2.3.3 Semiconductors 10
  - 2.3.4 TACIT Detectors 17

3 Devices 18
- 3.1 Antenna-coupled and Reflection-coupled Devices 20

4 Device Fabrication 24
- 4.1 Lithography 26
- 4.2 Etches 29
- 4.3 Metal Deposition 33
- 4.4 Device Testing 36
  - 4.4.1 TLM Patterns 36
  - 4.4.2 Probe Testing 37
- 4.5 Mounting 39

5 Measurement Techniques 40
- 5.1 Electrical Measurements 40
  - 5.1.1 Capacitance-Voltage Curves 41
  - 5.1.2 Current-Voltage Curves 42
  - 5.1.3 Tuning 43
- 5.2 Optical Measurements 46

5.2.1 Transmission 46
5.2.2 Photoconductivity 47
5.2.3 Photovoltage 48

6 Photoconductive Results **50**
6.1 Results for the DSQB Sample 51
6.2 Results for the CC1 Sample 52
6.3 Bolometric model for photoconductivity 54

7 Gate Photovoltage Results **59**
7.1 Polarization 63
7.2 Chemical Potential 66
7.3 Comparing Model to Data 69
7.4 Relaxation Times 72
7.5 Problems with the Model 74
7.6 Detector Responsivity 76

8 Conclusion **81**

Bibliography **84**

A Intensity Calibration **91**
A.1 Measurements 91
A.2 Transmission Factors 93
A.3 Error Bounds 96

B Calculating Electric Field and Charge Density **97**
B.1 Electric Field 97
B.2 Charge Density 98

List of Figures

3.1 Heterostructures for wafers DSQB and CC1 19
3.2 Schematic of edge-coupled device 20
3.3 Schematic of antenna-coupled device 21
3.4 Schematic of reflection-coupled device. 23

4.1 Redeposited sidewall material on top of mesas 33
4.2 Pinholes in PECVD-grown dielectric 35
4.3 Transmission Line Model (TLM) of ohmic contacts 37

5.1 Schematic of the capacitance-voltage (CV) measurements. 42
5.2 Capacitance-voltage curve and the integrated charge density. 42
5.3 Schematic of the current-voltage (IV) measurements. 44
5.4 Schematic of the THz optical setup. 46
5.5 Schematic of the photoconductivity experiment. 48
5.6 Schematic of the gate photovoltage experiment. 49

6.1 Peak photoconductive signal height at several temperatures. 52
6.2 Normalized transmission for the CC1 sample at 15K 53
6.3 Photoconductive signal for the CC1 sample at 15K. 54
6.4 Peak photoconductive signal measured at a range of temperatures. . 56
6.5 Calculated product $T_{eng}(1/R_{SD})(dR_{SD}/dT_e)$ for the bolometric model 56

7.1 Gate photovoltage peak signal and relative transmission for the CC1 sample, tuning through the intersubband transition. FEL frequency is 103cm^{-1}. 60
7.2 Circuit model combining the effects of the photo-induced changes in capacitance and chemical potential. 61
7.3 Chemical potential as a function of temperature for several charge densities 68
7.4 Gate photovoltage data, at 10K. 70
7.5 Calculated values for the gate photovoltage using the extracted relaxation times. 78

7.6 Calculated contribution to the photovoltage from the polarization effect, using the extracted relaxation times. 78
7.7 Calculated contribution to the photovoltage from the chemical effect, using the extracted relaxation times. 79
7.8 Absorption coefficient, in cm^{-1} 79
7.9 Relaxation times extracted from the combined model. Open circles are the points for which the model equation had no solution. 80

A.1 Optical setup with Thomas-Keating detector for calibration of reference detector. 93

List of Tables

4.1 Standard process segments used in all processing. unless otherwise noted. 25
4.2 Process sequence for log-periodic antenna-coupled detectors. 26
4.3 Process sequence for reflection-coupled detectors with dielectric layer. 28
4.4 Process sequence for edge-coupled detectors with 4mm wide gate. made using mask CCM8. 30

7.1 Polarity of the terms in Equation 7.0.6 for the gate photovoltage modeled for samples CC1 and DSQB. 62

A.1 Parameters used in the intensity calculations 94
A.2 The relative errors in the calibrations of several powers used in device calculations. 96

Chapter 1

Introduction

The initial motivation for this project came from earlier work in Mark Sherwin's research group on nonequilibrium and nonlinear optical processes in semiconductors. The available detectors in the Terahertz (THz) frequency range (1 THz = 10^{12} Hz) that were sensitive enough to record the phenomena being observed were not fast enough to give as much time resolution as desired. The idea that came about was to use some of the phenomena that were being studied, but in the low-power, linear regime, and turn them around to use them as detectors. Such devices would inherently be fast enough to observe similar phenomena. In this manner, this project was started, to make THz detectors from semiconductor quantum well heterostructures.

Semiconductor quantum well structures have had a rich history of physics investigation ever since it became technologically feasible to grow them. Many phenomena have been implemented and studied in quantum wells, such as the quantum Hall effect and excitons. Quantum well heterostructures are now used in a wide array of commercial devices, from high-mobility electron transistors (HEMTs) to infrared night-vision cameras, to laser diodes. Even as some of these products reach mature commercialization, there is still strong interaction between new scientific research and technological development. For example, ongoing studies of scattering and relaxation processes in superlattices helped lead to the recent success in making the

first THz-frequency quantum cascade lasers. Semiconductor band engineering, materials growth techniques, and fabrication processes allow a high degree of control over the geometry and operational parameters of devices. This flexibility will undoubtedly allow semiconductor quantum well devices to have a rich future in both science and technology.

This work focuses on both technology and science through making and studying quantum-well-based detectors for THz-frequency light. The detectors are a new kind of voltage-tunable direct detectors, that in future iterations may be used for astronomical observations. The devices that have been fabricated and tested demonstrate that their physical detection mechanisms can be successfully implemented and used at temperatures well above that of liquid helium. Higher operating temperatures open the possibility that detectors of this kind could be used without having to fly liquid helium on space-born astronomical observing missions. The detector devices also offers a well-controlled system to study hot electron dynamics, particularly the subband population time from the excited to the ground subband in the quantum well. Understanding the processes that affect relaxation times is not only interesting for its own sake scientifically, but will also allow tailoring of the operating temperature characteristics of future iterations of far infrared detectors.

In this dissertation, the state of THz technology will be discussed, focusing on current developments in the kinds of detectors that are used at frequencies around the THz range. Then the detectors in this study will be presented, and the fabrication processes used to make them will be discussed in detail. A summary of the experiments conducted is given, including the electrical and optical measurements. Then the next two chapters present the results of the photoconductive and gate photovoltage measurements, and discuss the models used to explain the observed phenomena.

Chapter 2

Background

Technology development in the THz frequencies is improving at a rapid pace. Historically, technological development in this frequency range lagged that in the microwave or near-infrared ranges. This lag was due in part to the strong absorption of water vapor in air and the lack of strong, compact sources, such as the transistor oscillators or semiconductor lasers used at other frequencies. With the transformation of femtosecond-pulse THz generation into a standard laboratory technique and the very recent realization of quantum cascade lasers in the THz range,[24] progress is well under way toward making commercially-available THz sources with moderate power output. These developments will surely spur further THz technology development and commercial applications.

2.1 THz Technology

The THz frequency range ($3THz \Leftrightarrow 100cm^{-1} \Leftrightarrow 100\mu m \Leftrightarrow 12meV$) falls in the technology gap between electronics with high frequency transmission lines and waveguide techniques for microwaves and optics with free-space or fiber-based techniques for the infrared. Most materials are too lossy to be effectively used for transmission lines, and are too absorptive to be used for lenses for THz electromagnetic waves. In the UCSB Free Electron Laser (FEL) lab, THz light is generally ma-

nipulated with free-space optics with beam steering and focusing accomplished by gold-coated mirrors.

An important driver of advances in THz technology is astrophysics. The THz frequencies are one of the last areas of the electromagnetic spectrum to be investigated, but a number of phenomena are expected to have signals in this range. Such phenomena include blackbody emission (1 THz is the frequency of peak blackbody spectral intensity at 10 K), such as from dust particles, and numerous spectroscopic lines, from molecules and red-shifted lines from the time of the early universe. Observation in the THz range would also improve the analysis and interpretation of observations at other frequencies. One such case is in the treatment of dust. Dust clouds coming between the Earth and luminous objects can absorb and emit light, changing the temperature of the blackbody spectral distribution and possibly adding or damping spectral line features of the observed objects. These effects of dust have often been treated in a simplistic fashion, or sometimes even ignored, in many studies leading to problems in interpretation, such as pointed out in Ref. [4]. Improved observational capability in the THz frequency ranges would alleviate many of these problems. In the last decade, specifications for planned astronomical experimental systems have focused THz technology development on heterodyne receivers, which has in turn led to great advances in source, frequency multipliers, and especially in detectors.

2.2 THz Detectors

All that is needed for a detector of electromagnetic radiation is to have an element of the detector that is changed by absorbing or interacting with the light, and an element that registers this change in a way that is observable in the macroscopic world. These elements of a detector could be two different components or the same component could act as both. For example, a very simple THz detector would be a thermometer in a glass of water. The water is the THz absorber, and the thermometer

registers the change in temperature.

THz detectors have been made out of a wide variety of materials, including superconductors, pyroelectric materials, and semiconductors. Most detectors are two-terminal devices, where the detection signal is coupled out of the active region of the device on two leads. Most antenna-coupled devices designs also use only two terminals. There have also been reported several transistor-style detectors designs with three[12, 34]. The extra terminal is generally used to tune the operating characteristics of the devices, such as absorption frequency. To the best of my knowledge, there have not been any planar four-terminal antenna designs reported in the literature.

Both direct detection and mixing are used in the THz frequencies. In direct detection, the detector responds to only the signal beam. In a mixer, the signal beam is combined with a beam from a local oscillator (LO) at a frequency close to the signal frequency. The mixer detector responds to the superposition of the two oscillating electromagnetic fields with the detector output at the difference frequency. The input frequencies in a mixer are often referred to as the radio frequency (RF) and the difference frequency is also called the intermediate frequency (IF).

$$\begin{aligned}
V_{superpos}(t) &= V_{signal}\cos\left(\omega_{signal}t\right) + V_{LO}\cos\left(\omega_{LO}t\right) \\
P_{superpos}(t) &= {V_{superpos}}^2/R \\
P_{superpos}(t) &= \frac{V^2_{signal}}{R}\cos^2\left(\omega_{signal}t\right) + \frac{V^2_{LO}}{R}\cos^2\left(\omega_{LO}t\right) \\
&\quad + \frac{V_{signal}V_{LO}}{R}\left\{\cos\left[\left(\omega_{signal}+\omega_{LO}\right)t\right] + \cos\left[\left(\omega_{signal}-\omega_{LO}\right)t\right]\right\}
\end{aligned} \tag{2.2.1}$$

All detectors have a general tradeoff between speed and sensitivity. As direct detectors are generally optimized to be sensitive, they also tend to be slow. Mixers, on the other hand, must be able to respond quickly. The response speed of the mixer detector element is what limits the IF bandwidth, or how far away from the signal frequency the LO frequency can be. The superposition of electric fields allows the signal beam to be effectively amplified by the power of the LO beam, allowing mixers to recover the sensitivity traded off in order to make the detectors fast. This sensitivity comes at the price of introducing a quantum noise limit in the mixing

process. Thus, it is possible to make direct detectors that are more sensitive than mixers, even at arbitrarily high LO power. Direct detectors are generally favored in applications where ultimate sensitivity is needed because there is no such minimum noise threshold. The narrow IF bandwidth of mixers makes them preferable for spectroscopic applications, and mixers have been used in cases where sufficiently sensitive direct detectors were not available. More information about mixers can be found in the pivotal theory by Tucker,[43] developed for SIS superconducting mixers but applicable to mixers in general.

2.3 Survey of THz Detector Types

2.3.1 Superconductors

The dynamics of quasiparticles and Cooper pairs in superconducting materials has given rise to several detection mechanisms, including SIS tunnelling and bolometric change in resistance. Controlling material purity and uniformity has been important in achieving the thin film characteristics needed for the devices, especially maximizing the critical temperature for a given film thickness. The current state-of-the-art detectors are all made with low critical temperature materials. Detectors have been made from high temperature superconductors as well, to try to make detectors operable at temperatures well above 4K, but at present materials issues strongly limit their performance.

SIS Detectors

The dynamics of quasiparticles in superconductors give rise to a number of different detectors for the THz frequency range. Among these, a workhorse for frequencies below 1 THz is the superconductor-insulator-superconductor (SIS) detector. In SIS devices, a layer of an insulating material, sandwiched between two layers of superconducting materials, controls the tunnelling of quasiparticles between the

superconductors. These detectors, usually used in mixers, can be very sensitive. For frequencies up to a few hundred GHz, SIS mixer sensitivities can be near the quantum limit, with less sensitivity at higher frequencies. The quantum limit provides a minimum SSB system noise level of hf/K_B due to the quantum-mechanical properties of photons, and the quantum limit and noise temperature for mixer systems are discussed in detail in Reference [23]. In a single-sideband (SSB) mode, a heterodyne receiver only detects useful signal at the signal RF frequency on one side of the local oscillator frequency. In a double-sideband mode, useful signals are detected at both the signal frequency and its image on the other side of the local oscillator frequency ($\omega_{RF} = \omega_{LO} \pm \omega_{IF}$). For a a noise source that emits equally in both the signal and image frequencies, the SSB noise temperature will be twice that of the DSB noise temperature. From the recent literature, Jung-Won Lee and coworkers report a SIS receiver with 40-50K double-sideband (DSB) receiver noise temperature for 85-115 GHz, for use on the SRAO telescope[28]. Chattopadhay et al report a noise temperature (T_n) of less than 115K DSB at 528 GHz for both polarizations of a dual-polarization Nb SIS mixer with a crossed-dipole slot antenna[9]. At higher frequencies, Kooi et al report a noise temperature T_n=205K at 800 GHz and 410K at 900 GHz for NbTiN-based SIS receivers for the Caltech Submillimeter Observatory[26]. This rapid increase of the noise temperature as the detector frequency approaches 1 THz is typical of SIS mixers reported to date. SIS mixers require moderate LO power, of order microwatts. The frequency range of SIS mixers is limited to a natural cutoff frequency, f_{cutoff} that is approximately twice the superconducting energy gap, $2\Delta \approx 3.5 K_B T_c$ for temperatures well below the critical temperature T_c (from Reference [43] cited in Siegel's review article [41]). For a common material system, Nb-AlO-Nb, the critical temperature $T_c = 9.3$K and $f_{cutoff} \approx$ 1.3 THz. Materials with higher T_c, such as NbN (T_c = 16 K) or YBCO ($T_c > 90$ K), have potential for use above 1 THz, but currently junctions made from these materials are leaky or are of insufficient interface quality to realize this potential yet.

Superconducting bolometers

Another major category of detectors is the superconducting hot-electron bolometers (HEBs), including the transition-edge superconducting (TES) detectors. In these detectors, normal-state electrons absorb the THz light via free electron heating. The temperature is read out by biasing the device into the superconducting-normal state transition where the resistance strongly depends on the temperature. The sharpness of this transition makes these detectors very sensitive. Using the superconducting transition to read out the temperature change, TES detectors operate at lattice temperatures near T_c (for example, 9K for thick Nb films) or colder, to below 1K. To heat the superconductor into its transition range, many TES mixer designs use LO power and Joule heating with a DC bias, sometimes used in a feedback loop. Since free electron absorption does not have any frequency cutoff, these detectors are broadband. The frequency limits of these detectors are generally set by their antenna circuits, but wideband antenna designs such as the log spiral or double dipole allow mixers to be made where the intermediate frequency is only limited by the speed of the detector.

Superconducting hot electron bolometers in the literature can be broadly categorized by their dominant thermal dissipation mechanisms, phonon-cooling and diffusion cooling. With phonon-cooling, the electron gas transfers thermal energy to the lattice by coupling to phonons. The lattice then transfers heat to the host substrate throughout the area of the device when the superconducting film is deposited on a bulk substrate, as for mixers, or through the narrow beam supporting leads when the film is on a suspended structure, as for many direct detectors, especially the spiderweb bolometers. Examples of recent results for phonon-cooled devices operating above 1THz are given in References [27, 22, 51, 18]. The thermal time constant for bolometers can be expressed as the ratio of the specific heat and heat conductance, $\tau = C/G$. For mixers this time must be short to allow a wide IF bandwidth, so for a given size sample, the conductance is made large. For direct detectors, where sen-

sitivity is maximized, the conductance is much smaller. For phonon-cooled mixers, the limit on the IF bandwidth is set by the electron-phonon coupling. Diffusion-cooled mixers get around this limitation by allowing the hot electrons to diffuse into the metal of the electrical contacts. To be effective, the superconductor active region between the metal leads must be around or less than twice the electron diffusion length. For high-quality superconductor materials this requires submicron device lengths for IF bandwidths of a few GHz. Diffusion-cooled mixer designs generally can have larger IF bandwidths, but require more difficult device processing, than phonon-cooled devices. Measurements of diffusion-cooled devices for use above 1THz are given in References [31, 21]. An interesting point to note is that semiconductor heterostructures have much larger electron mobilities than even high-quality superconductor materials, so diffusion-cooled semiconductor devices could be made with larger dimensions, allowing much easier fabrication.

After a decade of big improvements in superconductor-based mixers, the advances in materials growth and processing and the advances in modeling that yielded these improvements are now being applied to direct detector systems. Most notable among recent efforts are the devices proposed and made by Boris Karasik and coworkers at JPL, discussed in References [19, 20] By using disordered superconducting materials, the electron-phonon relaxation time can be engineered to be very long, up to 1ms. The predicted sensitivity for near-THz-frequencies is very good, with the noise equivalent power (NEP) $\approx 10^{-20} W/Hz^{1/2}$ with a 1ms time constant at 0.1K operating temperature. Results from prototype detectors are in general agreement with expected behavior for these materials, so the next iterations of these detectors may soon approach the predicted sensitivity. If so, then these superconducting hot-electron bolometer direct detectors will compete favorably with the composite bolometers that are currently being used for high-sensitivity direct detection systems in the THz frequencies. Two composite bolometers systems reported in the literature for the THz frequencies are a spiderweb mesh bolometer with an electrical noise equivalent power (NEP) of $4x10^{-17} W/Hz^{-1/2}$ and a 40 ms time constant measured

at 300mK[7] or a 32-by-32 element bolometer array for a 350μm(0.9THz) camera with a NEP of $2.9x10^{-17} W/Hz^{1/2}$[44]. Note that both the superconductor and composite bolometer technologies require cooling to sub-Kelvin operating temperatures.

2.3.2 Pyroelectric Materials

Pyroelectric detectors have long been used as broadband, room-temperature infrared detectors. A broadband absorber absorbs the light, heating up the pyroelectric material, changing its electrical polarization. The change in polarization causes a voltage drop to occur across the crystal. Reference [32] reviews current research efforts, which are focusing on multi-layer material structures, processing with porous silicon or sol gels, substrate membrane processing and mircromachining, and use of conducting polymers.[39]

2.3.3 Semiconductors

Semiconductor materials offer tremendous flexibility in device design. Epitaxial growth techniques, such as molecular beam epitaxy (MBE) and metal-organic chemical vapor deposition (MOCVD), allow atomic monolayer control over crystal growth and doping with very high quality materials possible. Band engineering of heterostructures and homojunctions gives access to tailor and control many design parameters, including charge density, frequency, mobility, and excited state population lifetimes. Mature semiconductor fabrication processes give the freedom and ability to make 2-D and even 3-D structures with feature sizes ranging from millimeters to nanometers. The ability to fabricate devices in parallel makes moving from single devices to arrays straightforward. Semiconductor detectors dominate over large stretches of the electromagnetic spectrum, and detector technology in the THz frequency range is developing rapidly.

Schottky Diodes

Schottky diodes have been used for millimeter-wave detectors and frequency multipliers for several decades. In the THz range, whisker-contacted diodes are used at high frequencies due to their good sensitivity and their low parasitic capacitances. In a whisker-contacted device, a wire is brought down to contact the diode and often serves as an antenna. Although they are delicate, whisker-contacted devices have successfully been space qualified and flown. Current research efforts focus on planar diode designs made with semiconductor microfabrication methods, see Reference [10] for a review. Such devices give the benefits of mature semiconductor processing and allow for more integration of the detector with surrounding circuits, improving system performance. Multiple-diode circuits, such as balanced mixers, are easier and more compact to implement with planar diodes. Making arrays of diode detectors will be significantly easier for batch-processed planar diodes than for manual-labor-intensive whisker-contacted diodes.

Photoconductors

In photoconductive detectors, absorbed photons create electron-hole pairs, in the interband case, or excite electrons (holes) to conducting states, in the intraband case. An electric field is applied, and the current is proportional to the absorbed light. Performance of photoconductors based on bulk, 3-D materials has been limited by the material quality. Reducing the quantity of impurities is crucial for reducing the dark current and increasing the carrier recombination time. The extremely high purities that are needed can only be grown in a few facilities worldwide. For example, for Ge-based devices, essentially all the current state-of-the-art detectors presented at the recent international conference Far-IR, Sub-mm & MM Detector Technology Workshop used transmutation-doped Ge with impurity levels $N_D \leq 10^{13}\text{cm}^{-3}$ produced by Eugene Haller at Lawrence Berkeley National Laboratory[1]. These devices require the careful assembly of discrete components.

A one-dimension array has been made with stressed Ge elements, all compressed with a carefully-designed clamp to evenly distribute the stress to all the detectors equally.[38] Blocked-impurity-band (BIB) photoconductive detectors add a thick (of order 1-10μm) blocking layer to reduce the dark current. A typical structure is described in a recent work[14] by Goyal et al. The blocking layer allows the excited electrons to diffuse and be swept into the contact, but does not have impurity states. The carriers in the impurity band in the absorbing region are then trapped there, reducing dark current through tunnelling or diffusion.

Narrow Bandgap Semiconductors

HgCdTe and related HgTe alloys are important narrow-gap materials for detectors in the 1-30μmwavelength range. In semiconducting materials, photons with energies above the bandgap energy can excite interband transitions, creating an electron-hole pair. In a typical photodiode design, an applied bias voltage sweeps the electron and hole in opposite directions toward the electrical contacts. See Reference [37] for a review of recent advances in photovoltaic HgCdTe detectors. These detectors are highly successful around the 3-5μm and 8-12μm atmospheric windows. Steady advances in materials properties and growth techniques have allowed arrays with over 4,000 detector elements to be fabricated. Narrow bandgap technologies are limited in their application to the THz frequency range by the lack of materials with suitably small bandgap energies.

Quantum Well and Junction Detectors

The confined electron and hole states afforded by quantum well structures has led to a number of different kinds of detectors. These can be roughly grouped by the direction of electrical transport, in the growth direction, or in the plane of the quantum well.

Transport in Growth Direction Detectors where the excited electrons or holes travel in the growth direction to electrical contacts allow the carriers to absorb light in one region and travel to a region with a different band structure. In this manner, for example, electron-hole recombination and re-emission of the absorbed photons can be decreased in surrounding regions with differing distributions of available energy states.

QWIPs Quantum Well Intersubband Photoconductors (QWIPs) have been very successful at shorter wavelengths, especially in the 3-5μm and 8-12μm wavelength ranges corresponding to the atmospheric transmission windows. In these detectors, an electron, confined in a quantum well in the conduction band, absorbs a photon, elevating it to an excited state, from which it may tunnel to a continuum state, and then is accelerated by the applied electric field. In bound-to-continuum designs, the excited state is at an energy above the top of the quantum well, for a fast detector response. In bound-to-bound designs, the excited state is still confined within the quantum well, and the excited electron must tunnel out to contribute to the photocurrent, but this design reduces the dark current from thermally-excited carriers. QWIPs have been made into sensitive arrays with as many as 256x256 detector elements. The absorption mechanism in QWIPs is through intersubband transitions, so only the light polarization in the growth direction of the wells couples gets absorbed. As these detectors are often produced in arrays, the polarization of the normally-incident light must be transformed in-situ. At these relatively-short infrared wavelengths, antennae are not practical, and instead gratings or v-grooves are commonly used. Both techniques detract from the optical coupling efficiencies of these devices. Some groups are working on QDIPs, using quantum dots in place of the quantum wells in a QWIP structure. In quantum dots, normal incident light can couple directly to the electrons, but the sensitivity of these devices is, so far, well below that of the quantum well devices. Multiple quantum well structures are commonly used to increase the absorption efficiency of the light. This contribution to

the overall sensitivity has to be balanced with the increased probability for carriers to be recaptured into a quantum well, which will decrease the mean transit time and can increase the generation-recombination noise.

Recent efforts to extend QWIP designs to longer wavelengths have been led by the groups of A. G. U. Perera at Georgia Tech[35] and S. Bandara and S. Gunapala at JPL[5][16]. In order to make structures that have sufficiently small intersubband transition energies, the height of the well barriers becomes much smaller than for IR designs. The reduced barrier yields a much higher dark current, with contributions from increased tunnelling out of the well and increased thermal ionization. The cut-off frequencies of QWIP detectors are currently in the range of 20-70μmbut with poor sensitivity at these long wavelengths. Also, the oscillator strength of the transitions decreases with increasing wavelength. In the THz frequency range, QWIP technology is not competitive with other technologies.

HIWIPs and HEIWIPs Homojunction (HEterojunction) Interfacial Workfunction Internal Photoemission (HIWIP, HEIWIP) detectors have been developed, and show promise at longer wavelengths than QWIPs.[36] HIWIPs operate by free-carrier absorption in an emitter layer, with the excited carrier then being photoexcited across a barrier and into the collector. The detection mechanism in HEIWIPs is similar, but with different materials in the heterostructure, such as AlGaAs and a heavily-doped GaAs emitter. The cutoff wavelength for HIWIPs is determined by the workfunction at the emitter-barrier interface, and for HEIWIPs by the workfunction at the emitter-barrier heterojunction, with both tunable after growth by the electric field applied across the junction. The HIWIP detectors developed to date have had larger dark currents than expected by theory, but the theory indicates the dark currents could be less than for QWIPs at the long wavelengths. Current HIWIPs and HEIWIPs are being developed around 20-30μmcutoff frequencies. At longer wavelengths, bandgap narrowing limits the cutoff wavelength. In Reference [36], Perera states that for low emitter doping, bandgap narrowing would give a bandgap

offset of about 9meV in addition to that given by the bare GaAs/AlGaAs interface. Perera does make two suggestions of how to possibly overcome this issue, but new materials designs will clearly be needed before HEIWIP detectors could be made to operate in the THz frequency range, regardless of their performance there.

Transport in the Plane of the Quantum Well Electrical transport in the plane of the quantum well allows devices to take advantage of the high electron mobilities possible in quantum wells, and aspects of two-dimensional transport such as current confinement.

Free Carrier Absorption Free-carrier heating with normal-incident light have been demonstrated by Yang, Yngvesson, and colleagues, who made both direct detectors and mixers at 94GHz with this mechanism.[49] Their mixer used the nonlinear temperature dependence of the electron mobility around 100K and were operated at temperatures from 20K to 100K. They also studied their structures in magnetic fields. Yngvesson has recently proposed[50] using the large diffusion length found in high-mobility semiconductor heterojunctions to make diffusion-cooled hot electron bolometer direct detectors and mixers. For a 0.8μmlong device, he predicted that relaxation times of order 1ps and IF bandwidths of 100GHz should be possible. M. Lee and colleagues have demonstrated diffusion-cooled mixers using GaAs/AlGaAs heterojunctions and have measured IF bandwidths up to around 20GHz.[29]

Resonant Absorption Mechanisms Resonant absorption by intersubband transitions was first demonstrated by Wheeler and Ralston in 1971, for holes in a p-type Si-SiO_2 surface inversion channel[46]. Detection was by photoconductivity measurements, with a decrease in conductivity observed with the absorbed light. The expected absorption was only $10^{-4} - 10^{-5}$ of the incident light, for one pass through the heterojunction.

High electron mobility transistors (HEMTs). while extensively used for amplifiers and other high-frequency electronics, have not been applied as THz detectors because the device transit times have been too long. However, plasma oscillations in these transistors have frequencies that can be in the THz frequency range, offering the possibility of using them for devices such as photomixer sources and detectors. Shur and Dyakonov propose a detector design and present results from a prototype device, discussed in Reference[12]. Peralta has shown THz-induced changes in the conductivity of a separately-depletable, weakly-coupled, double quantum well structure.[34] In this structure, a grating gate on the device surface both coupled the normal-incidence THz light into the device and depleted electrons from stripes of the upper quantum well under the grating. THz light resonant with plasmon modes in the periodically-depleted well changed the conductivity of the non-depleted lower quantum well.

Resonant-absorption mechanisms involving magnetic fields have also been reported. For example, in Reference [49], mentioned above, Yang et al report detection through cyclotron resonance as a second mode of operation for their detector. Thiele et al report cyclotron-resonance-induced photovoltage that is due to the temperature-dependent chemical potential[42]. Yang and Peralta have both reported additional detection mechanisms with magnetic-fields that are as of yet not fully understood.

Quantum Dot Detector

The quantum dot detector reported by Komiyama and colleagues[25] has generated much interest among THz researchers. In this device, a quantum dot in a strong magnetic field connects two electron reservoirs. The quantum dot has two Landau orbital levels, with opposite spins, that form two metallic circular regions that are separated by an insulating ring region that suppresses tunnelling between the two orbital levels. When a THz photon is absorbed, an electron-hole pair is created. The addition of an electron to the central level and a hole to the outer, lower energy level, shifts the chemical potential of each of the two levels with respect to the reservoirs.

The device parameters are such that the shifted potential of the outer, lower energy level lines up with the potentials of the two reservoirs, allowing many electrons to flow between them during the long lifetime of the electron-hole pair. In this manner, a single photon absorbed generates a current of many electrons, and single THz photons can be counted. The speed of this device is set by the electron-hole pair lifetime, which for the reported device is 1 ms.

2.3.4 TACIT Detectors

This current work is part of an ongoing project to make Tunable Antenna-Coupled Intersubband Terahertz (TACIT) detectors for use as mixers. Currently, the most sensitive detectors for THz frequencies all require cryogenic cooling to near 4K or to even subKelvin temperatures. Schottky diodes operate at THz frequencies up to room temperature, but have too high a noise temperature to be usable for sensitive astronomical observations. Liquid helium adds weight and cost to satellites, and limits the observing lifetime of the mission. Much more THz space science could be achieved on limited resources with detectors that do not need to be cooled below around 20K.[30] TACIT detectors are proposed to meet this need by combining the broadband performance (large IF bandwidths) possible with hot electron bolometers and the strong resonant absorption of intersubband transitions.[40] The devices discussed in this work are not designed to test the ultimate sensitivity of these detectors, but rather to serve as diagnostic prototypes.

Chapter 3

Devices

The devices studied in this work were designed to allow optical and electrical measurements to be made simultaneously, in order to study the physical processes involved in detection. A transistor structure was chosen with the THz light incident on the edge of the wafer and passing through the device between the source and drain. The devices were very large, by semiconductor device standards, with gate several millimeters long. This large active area provided an easily-measurable device capacitance which allowed the density of electrons to be determined in situ. This capability was one of the diagnostic tools used to study the physics of hot electron bolometric detection.

The devices were all fabricated from doped GaAs/AlGaAs quantum well heterostructures grown by molecular beam epitaxy (MBE) in Art Gossard's research group at UCSB. The devices were made from two doped $GaAs/Al_{0.3}Ga_{0.7}As$ quantum well heterostructures. One, CC1, has a 400Å-wide single quantum well, and another, DSQB, has a double asymmetric quantum well, with the wells of width 75Åand 85Å, separated by a 25Åbarrier. The materials structures for these two wafers are shown in Figure 3. There are two main operational differences between the two samples. The first is that wafer CC1 has a back gate quantum well, which allows the electric field and charge density in the active area to be varied indepen-

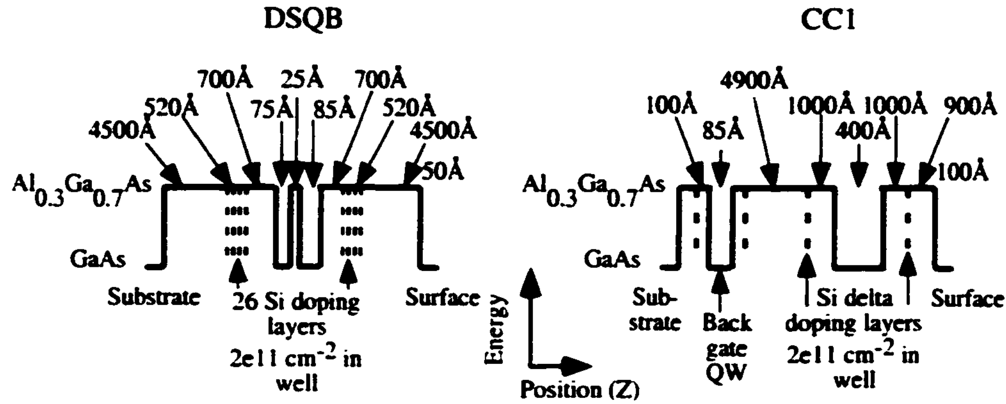

Figure 3.1: Material compositions of the two quantum well heterostructures DSQB (left) and CC1 (right).

dently, while these can only be changed together in the DSQB sample. The other is the slightly different frequency ranges over which they can be tuned, 84-115cm^{-1} (2.5-3.5 THz) for the DSQB sample, and 75-160cm^{-1} (2.3-4.8 THz) for the CC1 sample. In both wafers, electrons are supplied to each quantum well by silicon DX-centers in doping layers outside the wells. The structures are designed to have the first two subbands close together in energy, to absorb in the THz frequency range, and with the next subbands sufficiently far away in energy that absorption to these states can be ignored. The doping is chosen to only populate the first subband, so the two lowest subbands can then be considered to form a two-state system.

The wafers were patterned into transistor structures with one of three optical coupling geometries. All of the devices have source and drain ohmic contacts to the channel quantum well and an aluminum layer that forms a Schottky contact for the front gate. The three different optical coupling geometries implemented into devices are edge-coupling, reflection-coupling, and antenna-coupling.

All of the data and discussion presented in this work are for devices with an edge-coupling geometry, as shown in Figure 3. These devices have an aluminum layer on the back side of each device, which, with the front gate, forms a waveguide. The THz light is incident on the edge of the sample and travels in the waveguide between

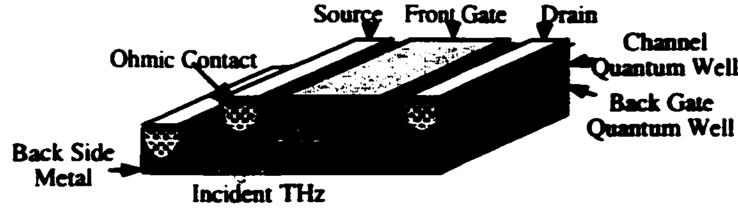

Figure 3.2: Schematic of device with edge-coupling geometry, processed from a GaAs/AlGaAs quantum well heterostructure. The THz light is incident on the side of the wafer and passes through the sample between the source and drain ohmic contacts.

the source/drain contacts. The devices made from wafer CC1 also had an etched region with an ohmic contact to the back gate quantum well. The devices were designed to be large enough to have an easily-measurable capacitance. Similarly, these devices were designed without antennae so that the bare detector performance could be studied.

3.1 Antenna-coupled and Reflection-coupled Devices

Previous devices were fabricated with antenna-coupling and reflection-coupling geometries. The first devices were made with a small active region and with a modified log-periodic antenna to couple the THz light. Figure 3.1 shows a picture of an antenna-coupled device, also called a Tunable Antenna-Coupled Intersubband Terahertz (TACIT) detector. The antenna design was based on a log-periodic antenna because that type couples to linearly polarized light at normal incidence. The design was modified to allow for the extra two electrical connections that were needed for the source and drain of the device in addition to the two gates. There were no four-terminal planar antenna designs available in the literature, so a simple modification to a typical two-terminal design was attempted. The extra metal connections were erroneously placed where the electric field of the antenna radiation pattern was maximum, rather than where the electric field was zero, as intended. This placement could have caused the THz oscillating fields from the main antenna leaves to capac-

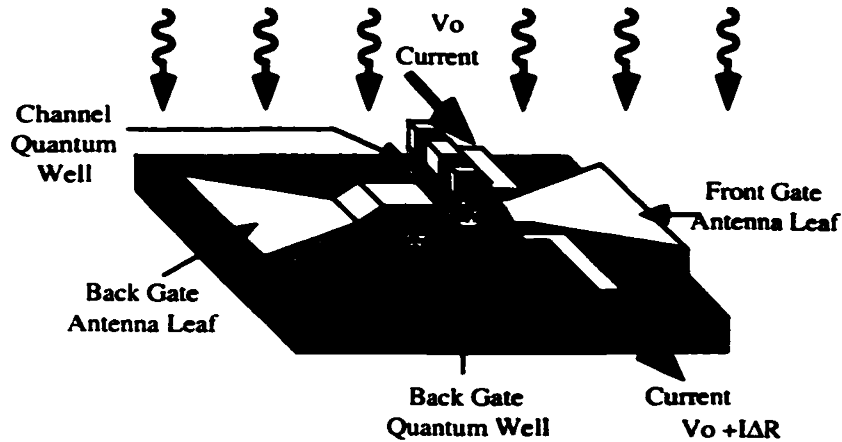

Figure 3.3: Schematic of device with antenna-coupling geometry. The two leaves of the antenna transform the THz polarization into the growth direction as well as carry the DC gate voltages.

itively couple or short to the source and drain of the device. These devices did not exhibit photoresponse. It could not be determined whether the cause was that the detector element did not work, or if the antenna design error kept the THz power from being delivered to the detector.

The second generation of detectors were designed to couple the THz light through a reflection geometry. A cartoon of this design is shown in Figure 3.1 and a picture of the central, active region is shown in Figure 4.3. By not using an antenna, the characteristics of the detector element could be isolated. In this device design, the active region is isolated from the surrounding area of quantum well by an etched trench. The front gate metal is deposited over both, such that the metal is continuous across the trench. In this manner, the active region of the detector and the surrounding quantum well area have the same electrical environment. There is no back gate in this design. The source and drain are connected to large contact pads at the edge of the wafer by gold wires that are evaporated on top of an insulating dielectric layer, with vias etched over the source and drain. Details of the fabrication process are outlined in Table 4.3. The quantum well area surrounding the active region is much larger, of order $10mm^2$, than the active area of the detector, of order

$10\mu m^2$. The larger size of the outer quantum well area gave it an easily-measurable capacitance, allowing CV characterization of the quantum well. Several of these devices were fabricated but only two were tested. Both devices had leaky gates, due to a processing issue that was solved for later devices.

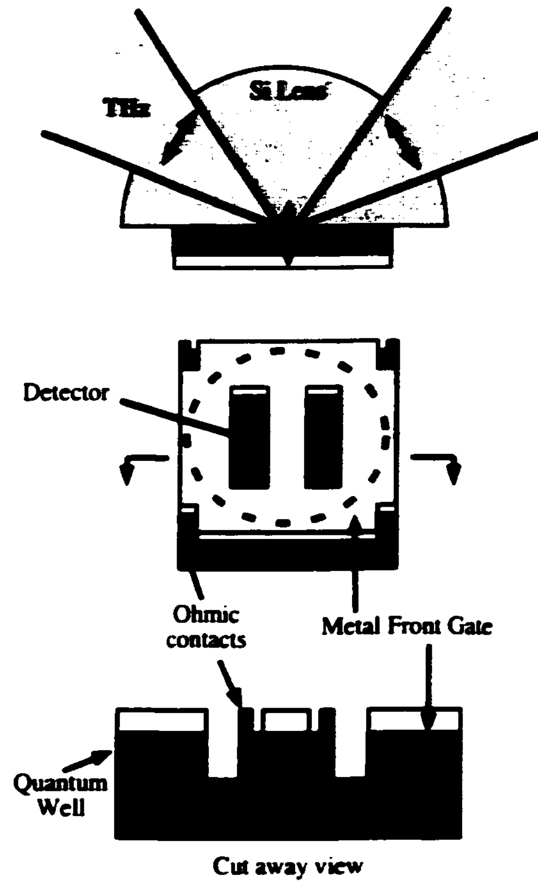

Figure 3.4: Schematic of a device with reflection-coupling geometry. The Thz light is incident on a lens or prism and passes through the substrate to enter the active region.

Chapter 4

Device Fabrication

All the detector devices were fabricated from GaAs/AlGaAs quantum well heterostructures in the UCSB cleanroom facilities. Each wafer was cleaved into pieces, and each wafer piece was put through a series of lithography, deposition, and etch steps to successively build up the layers of the devices. The fabrication processes that I developed to make several generations of detectors, with all the parameters I used, are listed in the process sheets, included as Tables 4.1, 4.2, 4.3, and 4.4.

Lithographic fabrication is an iterative process. Each stage of the process involves the same basic parts. First the sample is cleaned and dried. Photoresist is then spun on at high speeds, to form an even coating. It is baked to drive off some of the solvents, so that the photoresist will not ooze and will not stick to the mask. The sample is then aligned to a mask with an aligner, and the openings in the mask allow sections of the photoresist to be exposed with ultraviolet light. The UV light changes the polymers of the resist to make the exposed photoresist either more or less solvent in the developer compared to the unexposed areas, for positive or negative resist.[48] The sample is put in developer to dissolve the more soluble photoresist, leaving patterns of covered areas and clear areas. Once patterned, the sample is ready for an etch, metal deposition or the like. By successively repeating these steps, a device is built up in three dimensions, layer by layer.

Standard Clean :	5 min. each	
	5 min.	Acetone, room temperature
	5 min.	Methanol, warm, on hotplate setting "2"
	5 min.	Isopropanol, warm, on hotplate setting "2"
	1 min.	DI H_2O rinse
		N_2 dry.

Standard Lithography : Spin OCG 825 (4000 rpm, 30 s, 2.2 μm filter)
Bake 2 min. 5 s 95 °C hotplate
Flood expose 9 s at 7.5 mW
Spin 4110 (4000 rpm, 30 s, 2.2 μm filter)
Bake 2 min. 5 s 95 °C hotplate
Expose back and edge beads 2.5 min. at 7.5 mW
Pattern expose 8 s at 7.5 mW
Develop in AZ400K:H_2O::1:4 30 s total (2 beakers) with mild agitation.

Table 4.1: Standard process segments used in all processing, unless otherwise noted.

Sample Processing Record (5-26-1999 Process)

Sample ______________________________ Drawing

Stage	Date	What
Cleaving		Cleaving
Broad Mesa		Lithography (Standard)
Etch		Dektak : location __________ PR heights __________
		O_2 descum : 30 sec.
		Oxide etch : (NH_4OH:H_2O::1:10 30s) DI rinse 1 min.
		RIE #5 etches (want 2,000Å) DI rinse after etch
		clean chamber : O_2, 20mTorr, 10sccm, 200W, 10min
		calibration : Cl_2, 1.5mTorr, 3sccm, 50W,
		real piece : etch time __________
		Dektak : location __________ PR heights __________
Narrow Mesa		Lithography (Standard)
Etch		Dektak : location __________ PR heights __________
		O_2 descum : 30 sec.
		Oxide etch : (NH_4OH:H_2O::1:10 30s) DI rinse 1 min.
		RIE #5 etches (want 6,000Å) DI rinse after etch
		clean chamber : O_2, 20mTorr, 10sccm, 200W, 10min
		calibration : $SiCl_4$, 3mTorr, 10sccm, 100W, 6min

Sample Processing Record (5-26-1999 Process)	
	real piece : etch time ______________
	Dektak : location ________ PR heights ________
Top Metal	Lithography (Standard)
	O_2 descum : 30 sec.
	Oxide etch : (NH_4OH:H_2O::1:10 30s) DI rinse 1 min.
	Ebeam evaporation : 200ÅTi/3000ÅAu
	Acetone liftoff
	Probe testing ______________
Bonding Metal	Lithography (Standard)
	O_2 descum : 30 sec.
	Oxide etch : (NH_4OH:H_2O::1:10 30s) DI rinse 1 min.
	Ebeam evaporation (use bazooka) : 200ÅTi/10,000ÅAu
	Acetone liftoff
	Probe testing ______________

Table 4.2: Process sequence for log-periodic antenna-coupled detectors, made using masks CCM1, 2, and 3.

4.1 Lithography

Lithography is a critical component of any fabrication process as it is used in every step and defines the geometry of the devices. Most of the lithography was done with a two-resist process using OCG 825 and AZ 4210. Previously I had used just AZ 4210 or AZ 4110 with a toluene soak for liftoff processes, but kept having trouble with the metal at the edge of the liftoff region. It often did not break cleanly and stuck up from the surface, sometimes touching other metal surfaces. This double-layer process gave me much cleaner metallization edges, and I did not have the problem of the metal fins sticking up causing electrical shorts. I generally did the lithography for a process step on the same day that I did the actual fabrication process, but I made sure I always did so for metal depositions in order to get good liftoff.

Filtering the photoresists when applying them to the samples was important to reduce the amount of particulates in the resists, especially necessary for samples with small features. Each resist was filtered using a plastic disk filter and a syringe to force the resist through the filter. I used acetate filters, with a 0.22 μm pore size, and the 5cc syringes available from the Biology stockroom. It is possible that the acetate or syringe plastic reacted with the solvents in the resists, but even if that happened, it did not cause any noticeable effects in my processing.

Sample Processing Record (10-23-2000 Process)

Sample ______________________________________ Drawing

Stage	Date	What
Cleaving		Cleaving
Ohmic Contact		Lithography (Standard)
		O_2 descum : 30s
		Oxide etch : ($NH_4OH:H_2O$::1:10 30s) DI rinse 1min
		Ebeam evaporation : 108ÅGe / 102ÅAu / 63ÅGe / 236ÅAu / 100ÅNi / 3000ÅAu
		Acetone liftoff
		Anneal : 430 °C 45s hold time ____________
		Probe testing ____________
Mesa Etch		Lithography (Little Features)
		Dektak : location ________ PR heights ________
		O_2 descum : 30 sec.
		Oxide etch : ($NH_4OH:H_2O$::1:10 30s) DI rinse 1min
		RIE #5 etches (Want $\geq$3500Å) DI rinse after etch
		clean chamber : O_2, 20mTorr, 10sccm, 200W, 10min
		calibration : $SiCl_4$, 3mTorr, 10sccm, 100W, 4min
		real piece : etch time ____________
		Dektak : location ________ PR heights ________
Gate Metal		Lithography (Standard)
		O_2 descum : 30 sec.
		Oxide etch : ($NH_4OH:H_2O$::1:10 30s) DI rinse 1 min.
		Ebeam or thermal evaporation : 3000ÅAl $\geq$ etch depth
		Acetone liftoff
		Probe testing ____________

Sample Processing Record (10-23-2000 Process)

Deposit Dielectric	Lithography (Little Features)
	PECVD deposit 5,000ÅSiN_x (program sin50.prc)
	Put sample in ISO in ultrasonic for 10 seconds
	DI rinse and N2 blow dry
	PECVD deposit 5,000ÅSiN_x (program sin50.prc)
Dielectric Etch	Lithography (Little Features)
	RIE #3 etches
	clean chamber : O_2, 50mTorr, 20sccm, 500V, 20min
	sample : SF6 5sccm, O_2 2sccm, 10mTorr, 100V, 13min
	Microscope inspection ______________
Angled Evaporation	Lithography (Little Features)
	Ebeam evaporation at angle: 200ÅTi/3000ÅAu
	Acetone liftoff
	Probe testing ______________

Little Features lithography is the same as the Standard lithography, except that the mask pattern is exposed for 10s.

Table 4.3: Process sequence for reflection-coupled detectors with dielectric layer and metal contact lines to carry the source and drain contacts over the gate metal, made using masks CCM4, 5 and 6.

For developing, I used two beakers of AZ400K developer, diluted one part to four parts of water. I put the sample in the first beaker and agitated it gently for around 20s, and then moved the sample to the second beaker, again with mild agitation, for the balance of the 30s total development time. I used two beakers, rather than one, to ensure that the sample was exposed to fresh developer so that the exposed resist in the patterned areas would be fully dissolved away. When I was developing a lot of samples, with edge bead removal, the first developer solution would turn pink. I did not want any possible saturation of the developer to affect my lithography. I found that I could expose the edge bead and the backside of the wafer and then develop away the excess photoresist and then do pattern exposure and development without the unexposed photoresist being noticeably thinned. If I did a third 30s develop cycle

on a sample, though, sometimes pinholes or holes would open up in the unexposed photoresist areas and I would have to clean it off and start the lithography all over again. For that reason, when I needed to adjust either the exposure or development time for a sample, I would usually adjust the exposure time and keep the usual development time. In particular, for processes where I needed to open up small windows in the photoresist, I needed to change my pattern expose from 8s to 10s to fully expose the small features. The lengthened exposure tended to overexpose the large features elsewhere in the device, but that was not as important. Also, when using glass-substrate masks, such as those made with the MANN pattern generator on campus, the exposure times need to be longer than for quartz-substrate masks, such as around 10s rather than 8s.

4.2 Etches

Both wet and dry etches were used extensively in my processing. Wet etches were used for oxide removal and etching down to near the back gate for the edge-coupled sample process. Reactive Ion Etching (RIE) dry etches were used for creating mesas in the other processes and for etching dielectrics.

The wet etch I used the most was the oxide removal etch, $NH_4OH:H_2O::1:10$. Before most metallization depositions and etches, the oxide layer must be removed from the semiconductor surface to get rid of the insulating layer and avoid charge trap states. I try to get the sample into vacuum or into the AlGaAs etch as quickly as I can after the oxide removal etch, to minimize the amount of oxide that regrows. I have been told by some of the engineers in the cleanroom that a new oxide layer can grow back on GaAs/AlGaAs in about 10 minutes, but I have not checked that.

Lots of different etch solutions are available to etch GaAs/AlGaAs. Some have similar etch rates for AlGaAs and GaAs, while others are material selective. Early in my process development for the antenna-coupled devices, I investigated using anisotropic wet etches to get a ramp from the mesa top to the etched-away surface,

Sample Processing Record (8-28-2001 Process)

Sample ______		Drawing
Stage	Date	What
Cleaving		Cleaving
Mesa Etch		Lithography (Only the 4110 resist, as below) Dektak : location ________PR heights ________ O_2 descum : 30 sec. Oxide etch : (NH_4OH:H_2O::1:10 30s) DI rinse 1 min. Wet etch : etch times and depths ____________ NH_4OH:H_2O_2:H_2O::5.8:1:83::7.0ml:1.2ml:100ml) Dektak : location ________PR heights ________
Ohmic Contact		Lithography (Standard) O_2 descum : 30 sec. Oxide etch : (NH_4OH:H_2O::1:10 30s) DI rinse 1 min. Ebeam evaporation : 108ÅGe / 102ÅAu / 63ÅGe / 236ÅAu / 100ÅNi / 3000ÅAu Acetone liftoff Anneal : 430 °C 45s hold time ____________ Probe testing ____________
Front Gate Metal		Lithography (Standard) O_2 descum : 30 sec. Oxide etch : (NH_4OH:H_2O::1:10 30s) DI rinse 1 min. Ebeam or thermal evaporation : 3000ÅAl Acetone liftoff Probe testing ____________
Back-side Metal		Ebeam or thermal evaporation : 3000ÅAl
A/R Coating		Thermal evaporation : L/W______NiCr → ______Ohms

Table 4.4: Process sequence for edge-coupled detectors with 4mm wide gate, made using mask CCM8.

to bring metal from the mesa top to the etched area without breaks. I tried a variety of etches, but in the end decided that they all had too much undercut for the small mesas I was making at the time. The lateral undercut was often about the same size as the etch depth. So, where I was etching down about 6,000Å, the lateral undercut on both sides of a mesa a few microns wide tended to eat up the room I had left for alignment tolerances. That made my future alignments much harder, and the yield of future steps correspondingly lower. I also did not get as reproducible results from the etches as I wanted. Probably if I had better control over the etch solution conditions, especially temperature, I would have had better reproducibility. For the large devices I made later, I did not care as much about the undercut, and did use a wet etch to get access to the back gate quantum well for ohmic contacts. The etch I used in this case I got from Jon Williams, and I got good reproducibility with it. That solution did not heat up appreciably on mixing, unlike many of the anisotropic etch solutions I had used.

Reactive Ion Etch (RIE) processes offer anisotropic etches for many semiconductor and dielectric materials. RIE etches use a combination of chemical and physical etch mechanisms. A plasma is created, that then ionizes the target gas, which is then electrostatically propelled toward the sample. The energetic ions react chemically with the surface, but have directionally aligned momenta (typically normal to the sample surface) which gives the etch its anisotropy.

When I started developing a dry etch process for my GaAs/AlGaAs structures, I got etch characterization information from Mike Wanke. He had a series of etches with Cl_2, $SiCl_4$, and BCl_3 to characterize the etch rates and sidewall profiles. I did another characterization series, purposefully duplicating many of the combinations of parameters that he had used. I found that my results were quite different from his, and over time my etch rates would vary dramatically. Such behavior for the RIE #5 machine in the cleanroom is fairly typical, and is due in large part to what processes everyone else is doing in the machine, and whatever they end up coating the chamber walls with. I started doing an oxygen plasma clean cycle before every run, which

reduced the variability, but I always did a calibration test piece right before doing my depth-critical etches. On occasion, the etch rates I would get on a given day would be up to around twice the etch rates I normally measured. Day to day the etch rates varied, but all the runs on the same day had reproducible etch rates.

For the antenna-coupled devices, I needed to create a two-level mesa structure, with sidewalls that could slope, but did not have any undercut. I developed a process for a slow CL_2-based GaAs/AlGaAs etch for the first etch, and then a $SiCl_4/Cl_2$ etch for the second mesa etch. The first etch needed to go a specific depth, and had to have clean sidewalls, which forced me to use pure chlorine, even though that gave me the fastest etch rates. I reduced the etch rate by decreasing the quantity of chlorine atoms in the chamber, through lowering the pressure and flow rate. I still ended up with a pretty short etch time, such that a few seconds over made a big difference and it was important to do a calibration before this etch. For the second etch I could use a $SiCl_4/Cl_2$ mixture, which gave me straighter sidewalls and a slower, more controllable etch rate. The presence of the $SiCl_4$, however, caused material to be deposited on the sidewalls. This material also covered the edges of the top of the mesa, with a uniform width. The width of this layer of material on the top of the mesas was roughly the same for all the samples I processed, and was the same for different-sized mesas. At the corners, the material would show a raised stripe. Figure 4.2 shows this sidewall material covering part of the top of mesas in two samples. The left image is an optical picture of an actual device, processed with a $SiCl_4/Cl_2$ mixture. The right figure shows an SEM image of a test pattern that was etched using a BCl_3/Cl_2 mixture. This picture shows the deposited material, dark, on the lighter-colored mesa, and shows the ridges that develop pointing along the corners of the mesas. In the right of the photo some redeposited material is visible in the etched region. The first mesa etch had to have clean sidewalls or else the second etch would redeposit the sidewall material over the etched region like the grass shown. Also to reduce scum and grass, I followed Mike Wanke's advice to rinse my samples in water immediately after removing them from chlorine-based

Figure 4.1: Material redeposited on sidewalls and top of mesas. Left: from a $SiCl_4/Cl_2$ RIE gas mixture. Right: from a BCl_3/Cl_2 gas mixture. Note the angled ridges at the corners of the mesas.

RIE etches.

4.3 Metal Deposition

Several metal deposition steps are included in each of the processes. The simpler depositions are the gate metallizations and wiring layers. An oxide-removal etch was done just prior to each evaporation of metal onto bare semiconductor, as described above. Aluminum was deposited by evaporation by either thermal evaporation or ebeam evaporation for the front gate of the large-mesa devices. Aluminum was chosen over gold for the large gates because our group has historically had better Schottky gates with less leakage over time with aluminum. For antenna components or other device-level wiring, 2,000-3,000Åof gold was evaporated with 100-200Åof titanium used as a sticking layer. For contacts that would later be wire-bonded, 6,000-10,000Åof gold were deposited by ebeam evaporation to give a thick layer with good mechanical properties for wire bond adhesion.

Ohmic contact metallization was carried out using the six-layer recipe that Jon Williams used and that our group had originally obtained from Umesh Mishra's group. An oxide-removal etch was always done just before the ohmic metallizations. I would bring the ebeam chamber up to atmosphere while I rinsed the samples so that

I could immediately load the samples onto the sample stage and get the samples into vacuum quickly, usually within 12 minutes even when mounting multiple samples with shadow-mask pieces. The first four layers, Ge/Au/Ge/Au, form the AuGe alloy when annealed. The Ni helps the AuGe alloy diffuse into the semiconductor, and the top Au layer adds enough metal for mechanical stability. With this recipe, and annealing at 430 °C for 45s, I had good results, for making ohmic contact to a layer 2,000Åbelow the surface, but not contacting a layer 8,000Åbelow the surface.

When I deposited metal on edge-coupled devices or any sample where the device was not electrically isolated from the edge of the sample, I took special steps to keep metal from getting onto the sample edges. To protect the edges of the samples, I mounted them on glass cover slips with a small amount of photoresist and a quick hotplate bake. I used pieces of Si or glass to shadow-mask the edges of the samples and painted photoresist over the edge of the sample onto the glass cover slip. Otherwise metal would adhere to the side of the sample and to a thin line around the edge of the sample. Under high optical magnification, I could see that the photoresist would be removed right along the edges of the wafer in the develop step. I think that this was just from the developer dissolving away (laterally) a portion of the unexposed photoresist, which has a small but nonzero solubility. Metal evaporated into spalled areas, where the semiconductor had chipped during cleaving or in later handling, generally shorted or made bad diode-like electrical connections between quantum well layers and surface gate metal layers. Any metal on the edges of the sample or in such chipped areas that gets annealed will definitely short out the quantum well to any other connected metal areas. For the smaller devices, that were not edge-coupled, I always removed the photoresist edge-bead by exposing and developing it, leaving a rim around the sample wafer that always got coated with metal. The devices were electrically isolated from this metal region by an etched region that extended through all the quantum well layers. This etch-isolation was, for me, much easier and gave me better device yields than trying to mask all the edges of the sample during evaporations. This is one of the reasons I had better device yields

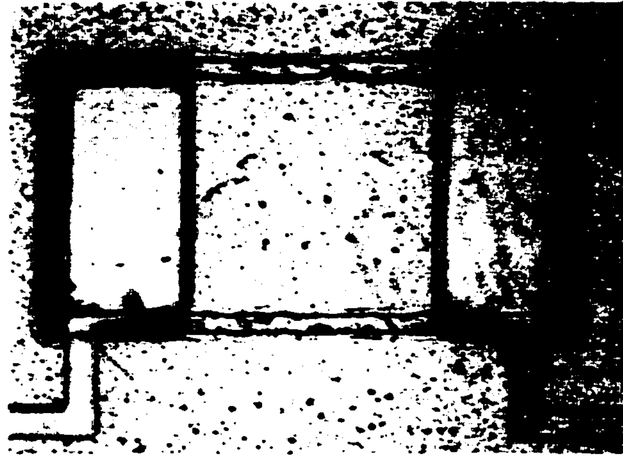

Figure 4.2: Picture of center region of reflection-coupled device showing the pin-holes in the SiN PECVD-grown to cover the aluminum front gate layer. The source and drain contact pads and leads to the mesa are less textured.

with the smaller, non-edge-coupled devices.

For cases where I needed to bring metal from one elevation to another, I used an angle-evaporation to coat one side of the mesa with metal. I mounted my samples in the adjustable arm in Ebeam #1, with the samples at around 60° with respect to the incoming spray of gaseous metal atoms. I always got good coverage and electrical connectivity between layers. At first I had tried to use the mesa itself as a shadow mask to break the metal on the side of the mesa away from the metal source, but found that about half of the devices did not have a break in the metal. My mesas, around 6,000Å tall, were too short to work well as shadow masks. Other people have gotten good results, but their mesas were 1-2μm tall. I ended up having to put a gap in my mask layer. When making a metal connection through a small hole in a thick dielectric layer, the higher the aspect ratio (layer height / window width), the more difficult it is to get good electrical connectivity. The aspect ratios should be kept well below 1 for reasonable yields.

Dielectric deposition was carried out using Plasma-Enhanced Chemical Vapor Deposition (PECVD). PECVD-grown SiN and SiO_2 have small pinholes, shown in Fig.4.3 that will allow subsequent metallization layers to contact layers below the

dielectric. The pinholes can be worked around by growing multiple dielectric layers, taking the sample out and putting it briefly in isopropanol in an ultrasonicator to change the surface morphology, so that later layers' pinholes will be unlikely to line up with the first layer's.

4.4 Device Testing

Devices were tested in the cleanroom after key steps, to determine which samples were good for continued processing, and which had problems. Also, all completed devices were tested on a probe station, at room temperature and at 77K in liquid nitrogen, either in the cleanroom or outside, prior to mounting for helium cryostats.

4.4.1 TLM Patterns

A standard way to determine the contact resistance of ohmic contacts is to test them in a Transmission-Line Model (TLM) pattern. The basic idea is to measure pairs of contacts in a configuration that allows the contribution to the total resistance from the contact resistance to be separated from that of the sheet resistance of the conducting layer. Figure 4.4.1 shows a TLM pattern of contacts, and a schematic side view of a pair of contacts. A TLM pattern has a series of pairs of contacts, all of uniform width, W, separated by different lengths, L. The resistance between a pair of contacts is modeled as two contact resistances, R_c in series with a sheet resistance, R_s. The sheet resistance is taken to be the resistance seen by current flowing between two planes at the edge of each contact that are perpendicular to the contacts. Between this plane, shown as a dashed line in the figure, and the metal of a contact, the resistance is modeled as a single contact resistance, R_c. The current is assumed to be limited to flow in the region between the contact pair, such as if the TLM pattern region was isolated from the rest of the semiconductor wafer by an etch. The current is also assumed to flow through the semiconductor between

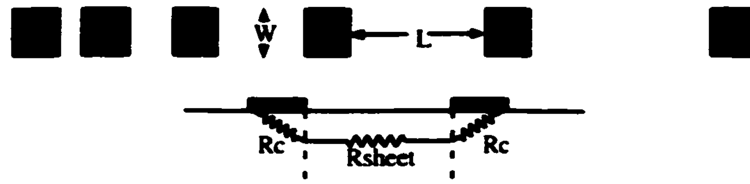

Figure 4.3: Top view of a transmission line model (TLM) pattern and schematic side view of a pair of ohmic contacts.

contacts in a layer of thickness t that is small compared to the separation length L, such as a doped region or a quantum well. With these assumptions, the resistance between a pair of contacts can be expressed,

$$R_{total} = 2R_c + R_s = \begin{cases} 2R_c + \rho_{s3D}\frac{L}{Wt} & : \text{For a 3D conducting layer} \\ 2R_c + \rho_{s2D}\frac{L}{W} & : \text{For a quantum well} \end{cases} \quad (4.4.1)$$

where ρ_s is the 3D or 2D resistivity of the bulk doped layer or quantum well respectively. In both cases, the sheet resistance is proportional to the ratio L/W, called the number of squares. If the resistances between pairs of contacts with different spacings, L, are plotted as a function of the number of squares between each pair, then the intercept of the resulting line will be $2R_c$ and the slope will be the 2D sheet resistivity, ρ_{s2D} or ρ_{s3D}/t. In this way, the contact resistance can be determined independently of the sheet resistance.

4.4.2 Probe Testing

All finished devices that had progressed successfully through all the processes were tested on a probe station prior to mounting for helium cryostats. They were first tested at room temperature, which is quick and easy, and then tested at 77K in liquid nitrogen. If a sample's contacts froze out at 77K, or there were other problems, then that sample would not be mounted for helium cryostats. Even though a sample that worked at 77K might still fail at 4K, weeding out bad devices at 77K saved much time in mounting and testing samples in helium cryostats. At each temperature, contacts were tested in pairs with several other contacts to check the properties of

each one and isolate which contacts are functional or bad. Contacts to a quantum well were checked to see that they were electrically connected, and to see how linear the current-voltage curve was. Contacts to the front gate were tested relative to the channel quantum well to see that the front gate was a good Schottky diode with the proper turn-on voltage, and to see if the diode was leaky, or allowed current to flow below the turn-on voltage. Contacts to the back gate were tested relative to the back gate, to verify they were electrically connected and ohmic, and then to the channel quantum well, to see if there was proper isolation between the two wells in the range of operating voltages.

Probe testing devices at 77K was done on a metal heat sink cooled by liquid nitrogen. The metal heat sink was usually a thick washer or optical post shim, and was placed in the cut-off bottom of a styrofoam cup. Liquid nitrogen was poured into the cup. The boiled-off nitrogen gas purged air out of the space within the cup. Once the heat sink and cup thermalized to 77K, the sample was placed on the heat sink. The sample would often move around as it cooled down, until the liquid nitrogen could wet the surface. Then the sample was positioned on the heat sink and the probe tips lowered onto the contact pads. It is important to keep refilling the liquid nitrogen in the cup to keep some liquid in there at all times, in order to keep the water vapor purged away from the sample. If the sample ices over, it is difficult to reliably make contact between the probe tips and the sample contacts through the insulating ice layer. In this case the sample should be warmed up, dried off, and then cooled again in the nitrogen-purged environment.

For a working device at 77K, the sheet resistance of the channel quantum well should be less than at room temperature, and the gates should not leak, but illumination by visible light can cause significant changes in the electrical behavior. Visible light has energies larger than the GaAs/AlGaAs band gaps, creating lots of electron-hole pairs. These extra electrons can be created anywhere in the heterostructure stack, allowing current to flow in the growth direction to the gates, as well as changing the charge density in the quantum wells and the nearby band structure. These

effects frequently cause the IV curves between the channel quantum well and either gate to be like that of leaky, hysteretic diodes, and even the in-plane quantum well IV curves can be diode-like and hysteretic. The sample should always be in as dark an environment as possible, with all lamps turned off, when taking measurements. However, it is necessary to have the lamp on when placing the probe tips on the desired contact pads, and at 77K the effects of illumination are persistent. With experience the effects of illumination can be discerned from the effects of a bad device.

4.5 Mounting

Once a sample tested well at 77K, it was mounted for testing in a helium cryostat. Samples were mounted onto copper mounts, that allowed optical access for either edge-coupling onto the edge of the wafer or coupling the THz light onto the backside of the wafer. The mounts were made of copper to have good thermal conductivity to remove heat from the samples, which was necessary when using a sample-in-vacuum but which was largely irrelevant for the flow cryostat where the sample was in helium vapor. Electrical connections from the sample mounts to the cryostat were made with Samtek pins epoxied into the sample holder with Stycast 2850. Electrical connections between the sample and the Samtek pins on the sample holder were made with gold wires. For the edge-coupled devices, the wires were attached from the sample directly to the Samtek pins, with the connections made either by silver paint or cold, pressed indium. On the antenna-coupled samples, there was an intermediate piece of insulating material with gold evaporated into stripes. Gold wires were wire-bonded from the sample to the intermediary and separate wires were indium-soldered, or sometimes silver-painted, from the intermediary to the Samtek pins on the sample holder.

Chapter 5

Measurement Techniques

The detectors were tested and characterized with an array of electrical and optical measurements. All the measurements were carried out at cryogenic temperatures in a flow cryostat. The electrical measurements characterized the in-plane transport properties of the devices, and the optical measurements investigated the interactions of the electrons with the THz light.

5.1 Electrical Measurements

Electrical characterization was carried out by measuring capacitance-voltage curves, and current-voltage curves over ranges of gate voltages and temperatures. These measurements were used to see that the components of each device functioned electrically as expected and to measure in-situ device parameters, including the charge density and in-plane resistance. All these measurements were carried out at several temperatures in the range of 10K to 49K and in a few cases up to around 100K in a flow cryostat.

For all these measurements, the sample was cooled to cryogenic temperatures in the dark. Black polyethylene filters were placed over all of the cryostat windows to keep visible and infrared frequencies from hitting the sample and exciting electron-hole pairs across the bandgap. Cooling in the dark ensures that the electron charge

density and distribution are determined by the silicon dopants, as designed. The channel and gate contacts all must not be left floating during the cooling procedure in order to have repeatable electrical conditions during cooling, and hence a repeatable charge density and electric fields. For all the measurements on these detectors, the gates and channel source and drain were all connected together, and were connected to the electrical ground. If a voltage bias had been applied to the gates, then the electric field across the heterostructure would result in a modified charge density in the well. If a voltage bias had been applied to the source and drain, then the different electric fields across the heterostructure nearer to the source or drain would have resulted in a built-in electric field between the channel contacts. Also, more electrons would be liberated from the silicon dopants on one side of the device, leaving behind a spatially-varying density of positively-charge ionized silicon DX centers.

5.1.1 Capacitance-Voltage Curves

The capacitance was measured between the channel quantum well layer and the front gate, which form a parallel-plate capacitor. The capacitance was measured with an AC technique over a range of DC front gate voltages from normal operating values to beyond where the channel quantum well is depleted of electrons. By integrating the capacitance from depletion to a given front gate voltage, the mobile charge present in the well at that gate voltage can be determined, as shown in Figure 5.2 There is still charge in the well when the capacitance shows depletion. The remaining electrons are trapped in puddles in potential fluctuations, without a continuous electrical path to the channel contacts. Jon Williams observed that these non-mobile electrons can still absorb THz light.[47]

For samples that had a back gate, care had to be taken to keep the back gate capacitance to the channel quantum well and front gate from affecting the front gate-channel capacitance measurement. The frequency of the AC voltage was set

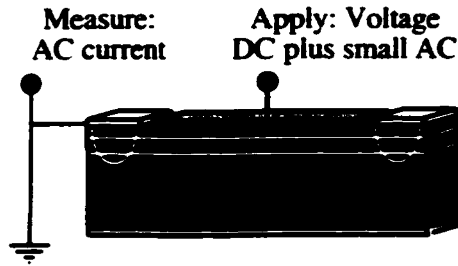

Figure 5.1: Schematic of the electrical setup for the capacitance-voltage (CV) measurements.

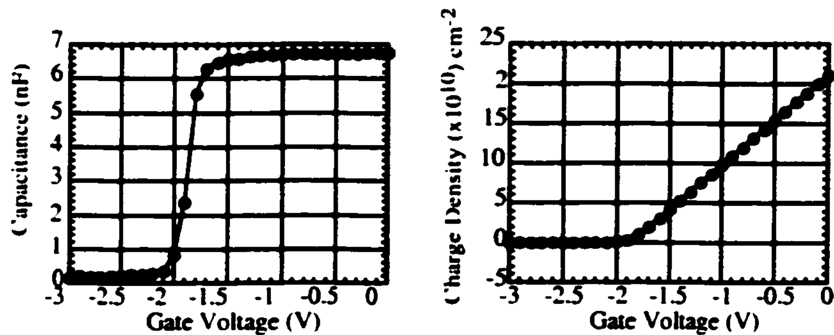

Figure 5.2: Capacitance-voltage curve and the integrated charge density.

low, at 34Hz. This frequency made the impedance between the channel quantum well and the back gate large enough that the AC current flowing from the front gate all went to the channel quantum well, without any appreciable current flowing to ground through the back gate. In this manner, the capacitive effects of the back gate in these measurements could be ignored. DC voltages were applied to the back gate, however, in conjunction with the front gate, to set the electric field across the well and the charge density in the well.

5.1.2 Current-Voltage Curves

The source-drain current-voltage (IV) curves give information about the electrical conditions in the well. The DC source-drain voltage is swept over a range of

values and the resulting current measured, as shown in Figure 5.3. Sets of IV curves were taken for different combinations of front and back gate voltages. Ideally, the contacts and active area of the quantum well would have only linear IV curves, pure ohmic behavior. In that case, the in-plane resistance can easily be found, which with the charge density from capacitance measurements, can be used to calculate the transport electron mobility. In these real samples, the IV curves had several deviations from ohmic behavior. The electric fields between the source and gates and between the drain and gates are different whenever the source and drain are biased to different potentials. When the gates bring the active region near to depletion, then the voltages applied to the source in the IV sweep may be enough to cause the region around the source to be locally depleted. Once any area is depleted, however, then the current flow is constricted or even turned off, and the IV curve changes slope to very high resistance. Where the charge density in the well was high, and all voltages well away from depletion, there still were non-linearities. There may be other effects of the spatially-varied electric fields across the device, as well as possibly from non-ideal ohmic contact behavior. The IV curves were generally not symmetric about zero volts applied, particularly at lower charge densities where depletion effects were more common. A relatively linear region was found to exist for bias currents around -100μA for most gate voltages. The bias currents for the photoconductive measurements were chosen to fall in this region so that these other effects would not affect the detection measurements.

5.1.3 Tuning

The presence of a back gate as well as a front gate in these transistor-like devices gives independent control of the electron charge density in the channel quantum well and of the electric field across the well. Just as the front and back gate voltages can be set independently, their voltages can equivalently be expressed in terms of the independent quantities of the charge density in the quantum well and the electric

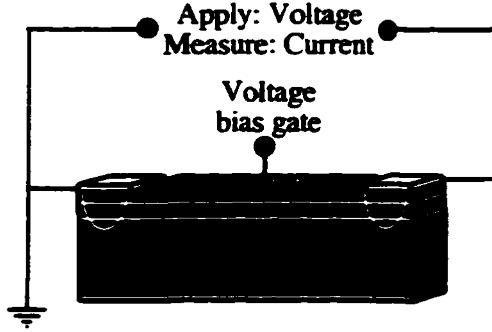

Figure 5.3: Schematic of the electrical setup for the current-voltage (IV) measurements.

field across the well. If the front and back gates are voltage-biased together, with the same polarity, with respect to the channel, then the charge density is varied. If the front and back gates are biased in opposition, then the electric field across the well will be changed.

The absorption frequency is tuned strongly by the electric field, through the DC Stark effect, but is also tuned by the charge density, through the depolarization effect. The depolarization shift is an increase in the absorption frequency from the bare subband energy separation due to internal excitations in the electron gas. When an electron undergoes a transition from the ground subband to the excited subband, the wavefunctions of all the electrons in the gas rearrange with Coulombic repulsion. The depolarization shift can also be thought of as a cross between a photon absorption and excitation of a plasma oscillation. The frequency shift depends on the difference in electron populations in the two subbands, $N_1 - N_2$,

$$\tilde{\omega}_{12} = \omega_{12}\sqrt{1 + \alpha\frac{N_1 - N_2}{N_s}} \qquad (5.1.1)$$

$\tilde{\omega}_{12}$ is the depolarization-shifted frequency, ω_{12} is the bare subband energy spacing, and N_1, N_2, and N_s are the first and second subband populations and the total electron population in the quantum well, respectively. α is the depolarization shift parameter, and is linearly proportional to the total charge, N_s, so $\tilde{\omega}_{12}$ just depends on $N_1 - N_2$. A full derivation of the depolarization shift is given in Reference [2].

In the detectors studied in this work, the quantum well structures are designed to have the Fermi energy fall between the first two subbands. At low electron temperatures but above zero, essentially all the electrons are in the ground subband, and the depolarization shift is maximum. At higher electron temperatures, for the same total charge, N_s, the proportion of electrons in the excited state approaches $1/2$, so $N_1 - N_2$ goes to zero and the absorption frequency approaches the bare subband energy spacing ω_{12}.

In all measurements, the voltages of all four terminals of the device, the source, drain, and both gates, must be kept in consideration. If the front gate is at too positive a voltage with respect to the channel, then current can flow across the Schottky barrier, irreversibly depleting the well. Similarly, if the back gate is at too positive a voltage with respect to the channel, then charge can tunnel through the AlGaAs barrier and ballistically flow in the growth direction to the channel or front gate. These two effects can happen for any portion of the channel. When a voltage or current is sourced across the source and drain, then the two channel contacts will have different potentials. Then the voltage differences and electric fields will vary across the channel in the plane of the quantum well. For a given measurement, once the current or voltage to be applied to the source and drain is chosen, the above considerations set the limits of gate voltages that can be set without losing the charge from the well. There can be other effects of the spatially-varying electrical conditions. One important example is the case of devices that have the back gate over the whole mesa while the front gate only covers a section of the mesa between the source and drain contacts. For these structures, it is possible to have the front and back gates set to voltages such that there is charge in the well in the region with both gates, but the area with just a back gate is depleted. In this case, there will be no current able to flow between the source and drain because the current cannot pass through the depleted areas around the contacts, irrespective of the conditions in the active area of the device.

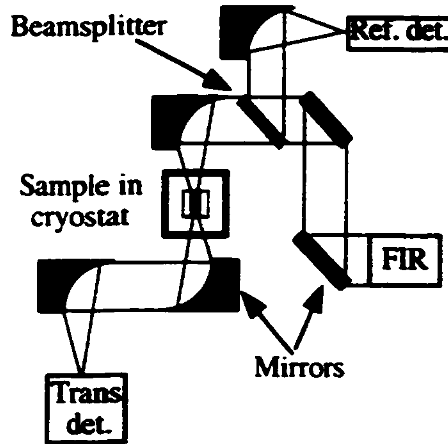

Figure 5.4: Schematic of the THz optical setup. The THz light traveled from the FEL port, through the beamsplitter where part was sent to a reference detector, and on through the sample with the transmitted THz light sent to another detector

5.2 Optical Measurements

Three kinds of optical measurements were performed on the detectors, transmission, gate photovoltage, and in-plane photoconductivity. All optical measurements were made with THz light from the UCSB Free Electron Laser (FEL). Measurements were carried out at more than one frequency, but all the measurements reported in this dissertation were made with the FEL tuned to 103 cm-1. The optical setup for these measurements is shown in Figure 5.4.

5.2.1 Transmission

The transmission through the sample was measured by collecting the light exiting the back face of the device focusing it onto a detector. By comparing the transmission of the device at operational gate voltages with transmission when the channel quantum well is depleted, the absorption due to the electrons in the quantum well alone can be determined. The attenuation coefficient is a measure of the

absorption per unit length of the sample,

$$\alpha = \frac{-1}{L} \ln \left(\frac{I_{full}}{I_{empty}} \right) \tag{5.2.1}$$

where L is the optical length of the sample, and I_{full}/I_{empty} is the ratio of the transmitted intensity when the quantum well is full of electrons to when the it is depleted. By varying the gate voltages, the intersubband transition can be tuned through resonant absorption of the fixed FEL frequency. The sample transmission was measured concurrently with each the in-plane photoconductivity and gate photovoltage. In this way, the photosignal can be compared with the absorption for the exact same set of FEL pulses. A comparison of the transmission and gate photovoltage measured concurrently while scanning the back gate voltage to scan the absorption through the FEL frequency is shown in Figure 7.1.

5.2.2 Photoconductivity

In the photoconductivity measurements, changes in the in-plane resistance of the channel were measured in the presence of the THz light. A current was sourced through the source and drain, and DC voltages were applied to the gates, as shown in the schematic in Figure 5.2.2. When the in-plane resistance of the device changed, the voltage across the source and drain would change accordingly, and the voltage pulse was sent to a preamplifier and then was viewed on an oscilloscope.

The level of the bias current was chosen to be as large as possible, since the output voltage pulse is proportional to the bias current, but while keeping the maximum voltage difference between the source and drain smaller than the applied gate voltages. Typical bias currents were in the range of -50μA to -150μA. The actual bias current for a given measurement was chosen after looking at the current-voltage curves for several sets of gate voltages and finding a region of currents where the IV curves stayed roughly linear. In these areas of parameter space, the resistance is well defined even if other regions of parameter space would deplete the quantum well or lead to other non-ohmic device behavior.

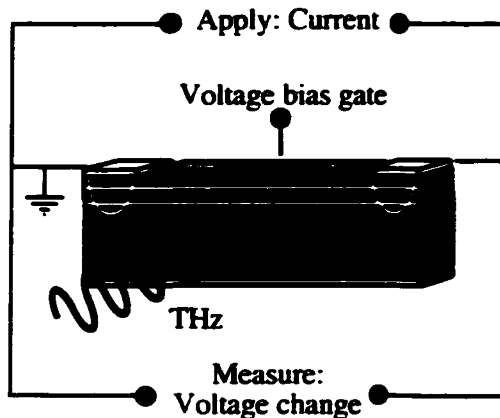

Figure 5.5: Schematic of the experimental setup for the photoconductivity measurements.

5.2.3 Photovoltage

In the gate photovoltage measurements, THz-induced changes in the front gate-channel capacitance are detected. When electrons in the channel quantum well absorb the THz light, they are excited to the upper subband. When the ground subband and excited subband have different expectation values of the position of the electron in the growth direction, labeled 'z', then there will be a net displacement of the electron gas in this direction. The separation between the two plates of the front gate-channel capacitor change, changing the capacitance. The front gate voltage, referenced to the unilluminated region of the channel quantum well which at ground, is sent to a preamplifier, and then to an oscilloscope. As shown in the schematic in Figure 5.2.3 and the circuit model schematic shown in Figure 7, there is a resistor in series with the front gate of the device. The time scales of the photovoltage measurements are much less than the resulting RC time constant, so the quantity of charge flowing to charge or discharge the capacitor is negligible.

If the heterostructure were perfectly symmetrical, then the expectation value of the position of the electrons would be the same for all subbands. The application of an electric field across the well breaks this symmetry, allowing a measurable gate photovoltage. Wafer CC1 is a symmetric 400Å-wide square quantum well as

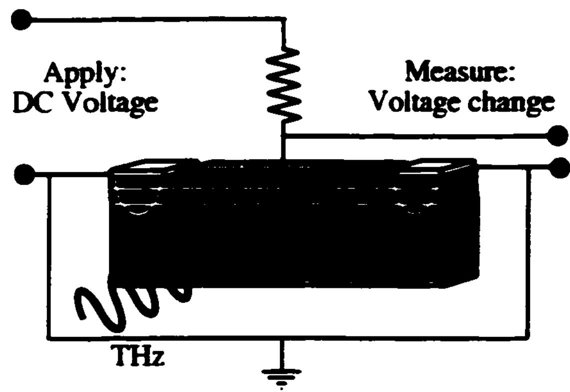

Figure 5.6: Schematic of the experimental setup for the gate photovoltage measurements.

designed, but with typical gate biases yields electron displacements of the same order of magnitude as wafer DSQB, an asymmetric double square well.

Chapter 6

Photoconductive Results

The photoconductive measurements looked at the resistance in the plane of the quantum wells under THz illumination. An in-plane bias current was applied between the source and drain contacts, and the voltage across these same contacts was measured. The pulsed THz light from the FEL heated the electron gas in the channel quantum well, decreasing the mobility, which resulted in a voltage pulse. The photoconductive measurements discussed here were taken with the incident FEL beam attenuated such that the intersubband transition was not saturated and only electron heating was observed. Under these conditions the photosignal pulses had decay times of order a few microseconds. With higher incident FEL power, the photosignal decay times were longer than 1 ms, which is attributed to lattice heating.

Prior experiments by Asmar[3] have investigated the photoconductivity of GaAs/AlGaAs heterostructures with THz illumination, but the polarization of the THz light was in the plane of the quantum well, so absorption was by non-resonant free carrier heating. Asmar used simultaneous photoluminescence and DC conductivity measurements in the presence of strong THz fields to determine the electron temperature and the temperature characterizing the energy distribution of longitudinal optical (LO) phonons. He found that for even the highest THz intensities employed, 12kW/cm^{-2}, the energies of electrons and LO phonons were each well

described by thermal distributions, and that the LO phonons had a 'hot' distribution determined by the electron temperature rather than the lattice temperature. In the experiments presented here, the incident THz polarization is perpendicular to the plane of the quantum wells, so that the photoconductive measurements are combined with intersubband transitions, a resonant absorption process. In this manner the photoconductivity will be more sensitive to low THz powers, making a better detection mechanism.

6.1 Results for the DSQB Sample

Photoconductive measurements were carried out on both the DSQB sample and on the CC1 sample called CC1-16. DSQB did not have a back gate, so the electric field and charge density could only be varied together, by changing the front gate voltage. At every gate voltage, a current was sourced through the source and drain and the peak of the photosignal response to the FEL pulse was recorded. The photoconductive signal was measurable over a wide device temperature range. The DSQB sample showed a photoconductive signal up to around 75K, with a maximum signal amplitude around 20K, as shown in Figure 6.3. A negative current was sourced, -20μA, so the negative photosignal indicates an increase in resistance, as expected for electron heating. The curve for a given temperature shows that the gate voltage tunes the intersubband resonance through the fixed FEL frequency (103cm^{-1}.) The peak absorption at the FEL frequency shifts to less negative gate voltages with increased temperature. The magnitude of the photosignal also changes with temperature. At low temperatures it increases, as the relative change in mobility with temperature increases. At higher temperatures, the magnitude decreases as the energy relaxation time is shorter, reducing the temperature change for a given amount of FEL power absorbed. A bolometric model of this behavior is presented later in this chapter.

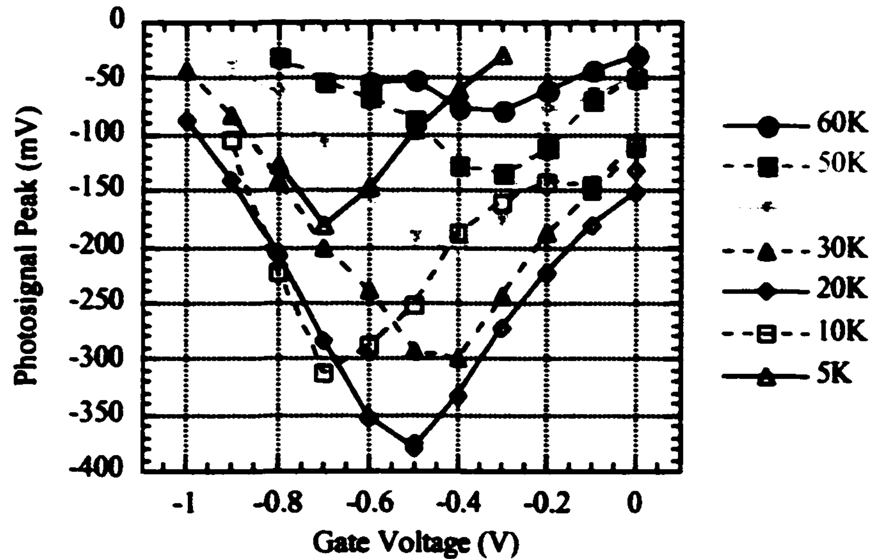

Figure 6.1: Peak photoconductive signal height for the DSQB sample, at fixed FEL frequency, at selected temperatures. Bias current applied was -20μA.

6.2 Results for the CC1 Sample

The CC1 sample had a qualitatively similar photoconductive signal to DSQB. I had intended to repeat the temperature scan from the DSQB sample on CC1, except to vary the back gate as well, so as to map out the photoconductive response with electric field and charge density each independently of the temperature. However, due to time constraints imposed by the FEL lab shutting down for renovations, a scan over a range of front and back gate voltages was only carried out for one temperature, 15K, shown in Figure 6.3, with a bias current of -150μA. For the temperature scan, the back gate was electrically grounded and only the front gate voltage varied. For the CC1 sample, photosignal was only detected to around 30K, but with the back gate grounded, the sample was not near resonance. The minimum normalized transmission (maximum absorption) for these data sets was 80-90% (20-10% absorption.) The transmission was normalized by the highest transmission measured, at gate voltages far away from resonance where there would be negligible absorption by the electrons in the quantum well. If I had been able to measure at resonance,

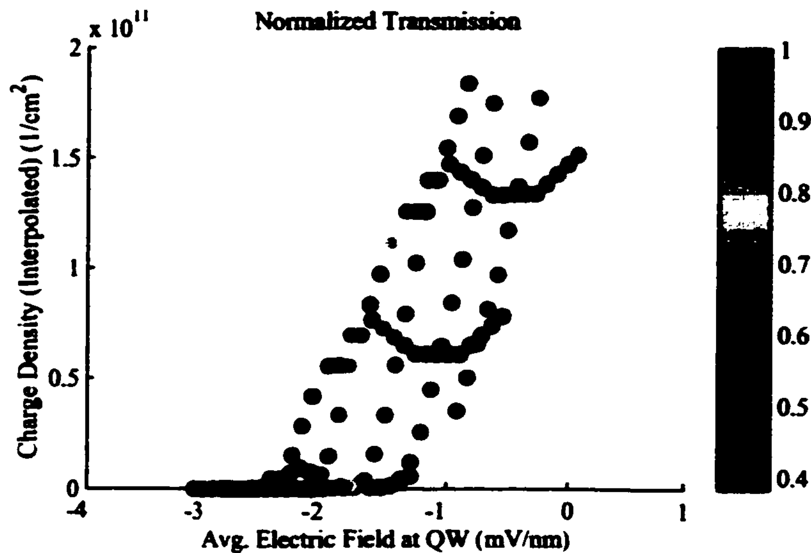

Figure 6.2: Transmission for the CC1 sample at 15K, normalized to the maximum transmission.

the signal would have been much larger, and I would have been able to detect the signal above the noise at much higher temperatures. In this data run, I also varied the incident intensity and the FEL pulse length. In comparison, the scan over back gate voltages at 15K included the low-charge-density region of resonant absorption. The minimum normalized transmission at resonance was 40% (60% absorption), the highest absorption I measured for any sample. It is interesting to note that the absorption and photoconductive signal were observable well into the regime where the quantum well was depleted of mobile charge.

In the gate photovoltage data runs, the minimum transmission at resonance was 70% (30% absorption) but the gate voltage spacing between data points was coarser than for the photoconductive data, so I may have been farther from the absolute resonance. Also, for both photoconductivity and gate photovoltage, strong photosignal is found for a region encompassing the resonant absorption and extending to lower charge densities. Strong absorption at low charge densities, seen in the photoconductive data sets, would help explain why the peak photosignals are centered at a lower charge density compared to the absorption. This shift is more pronounced at

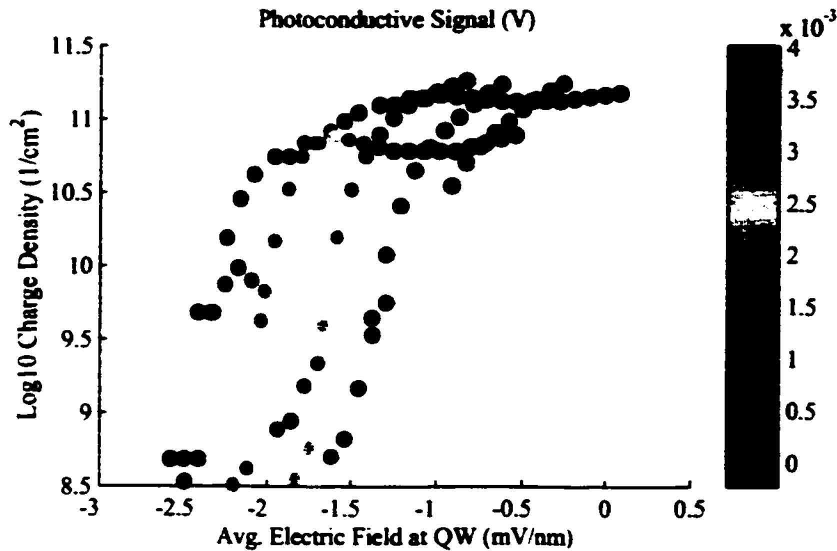

Figure 6.3: Photoconductive signal for the CC1 sample at 15K, with a bias current of -150μA. Significant signal was detected well into the regime where the quantum well is depleted of mobile charge.

higher device temperatures.

6.3 Bolometric model for photoconductivity

The observed change of in-plane resistance of these detectors is due to heating of the electron gas in the channel quantum well. The temperature dependence of the electron mobility is a composite of the various scattering mechanisms present, including from acoustic phonons, longitudinal optical phonons, and impurities. In the range of temperatures relevant for these detectors, the mobility decreases, and the resistance increases, with temperature. At the higher temperatures, there is stronger scattering, particularly from longitudinal optical phonons.

The responsivity of a detector is the ratio of the voltage output of the device to the incident power. In this electron-bolometric model, the detector responsivity, R, can be expressed in terms of the change of output voltage with electron temperature,

multiplied by the change in electron temperature with absorbed power,

$$\mathcal{R} = \frac{dV}{dP_{inc}} = \eta \frac{dV}{dT_e} \frac{dT_e}{dP_{abs}} = \eta \frac{V_{SD}}{R_{SD}} \frac{dR_{SD}}{dT_e} \frac{T_{eng}}{C_F} = \eta \frac{I_{bias} R_{SD}}{C_V} \left(T_{eng} \frac{-1}{\mu} \frac{d\mu}{dT_e} \right) \quad (6.3.1)$$

where η is the optical coupling, P_{inc} and P_{abs} are the incident and absorbed THz powers, T_e is the electron temperature, C_V is the specific heat of the electron gas, and T_{eng} is the electron energy relaxation time. V_{SD} and R_{SD} are the source-drain voltage and resistance respectively, and μ is the electron mobility. This equation assumes that the electron gas can be well described by a single electron temperature, T_e, and that the charge density in the quantum well is constant. Also, the lattice is assumed to not heat up, which is true at the low incident powers used in these measurements. From Equation 6.3.1, it can be seen that the responsivity is proportional to the product of the energy relaxation time T_{eng} and the relative mobility change factor, $(-1/\mu)(d\mu/dT_e)$. Note that for constant charge density, the relative change in mobility is just the negative of the relative change in resistance, $(-1/\mu)(d\mu/dT_e) = (1/R_{SD})(dR_{SD}/dT_e)$.

This bolometric model is compared to data for the DSQB sample. In calculating the bolometric product, the electron energy relaxation time, T_{eng}, was taken from measurements of the subband population time measured for another sample from the same double square quantum well heterostructure wafer[17] which found the subband population relaxation time, T_{pop}, ranged from 1ns for T_e=10K to 10ps for T_e=50K. The two relaxation times, the electron energy relaxation time, T_{eng}, and the subband population relaxation time, T_{pop}, are expected to be essentially identical for these samples because the dominant energy relaxation mechanism, emission of a longitudinal-optical phonon, also moves an electron from the upper to lower subband. Electron mobility values for the model were taken from the literature, see Figure 9.11 in Reference [11], for a sample with a low-temperature mobility similar to that for the DSQB sample, of order 10^5cm^{-1}/Vs. Figure 6.3 shows the resulting product, scaled by the source-drain voltage, device area, charge density, and K_B all for the DSQB sample. The last three factors come from the specific heat of

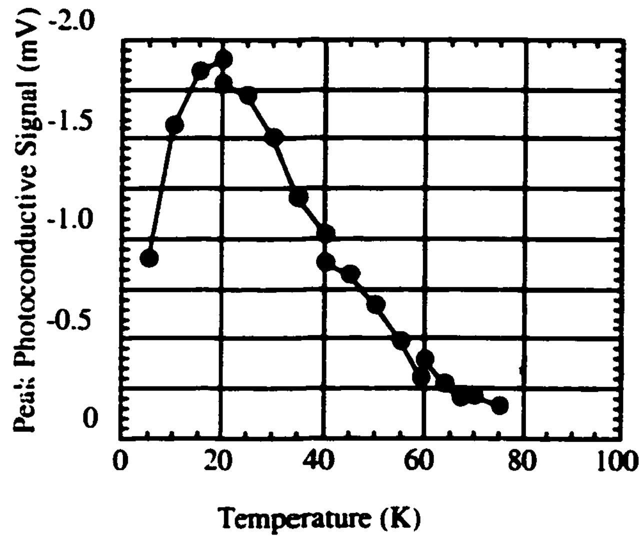

Figure 6.4: Peak photoconductive signal measured at a range of temperatures.

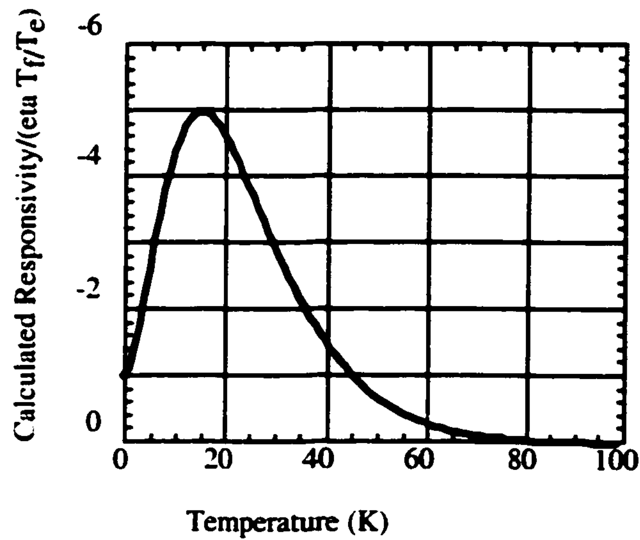

Figure 6.5: Calculated product $T_{eng}(1/R_{SD})(dR_{SD}/dT_e)$, scaled by bias voltage V_{SD}, device area, charge density, and K_B.

the two-dimensional electron gas, with quantum-mechanical Fermi-Dirac statistics, $C_V = AN_SK_B(T_e/T_F)$ where T_F is the Fermi temperature. In the electron-bolometric model, this scaled product is proportional to the responsivity via $\mathcal{R}/(\eta T_F/T_e)$.

The scaled product is in qualitative agreement with the peak photoconductive signal as a function of temperature, as shown in Figures 6.3 and 6.3. Some of the factors in the responsivity vary somewhat with temperature. For example, an increase in the mobile charge density with increasing temperature was observed in the capacitance-voltage curves for the DSQB sample, which affects the specific heat and the source-drain resistance. These additional temperature effects need to be added to make the modeling quantitative, but qualitatively, they may contribute to the difference in slope between the model and data at higher temperatures. Using our estimates for all these factors, ignoring the temperature dependence, however, equation 6.3.1 does give the correct order of magnitude for the measured data. For this DSQB sample, the optical coupling, η could only be estimated since the intensity had not been calibrated when the photoconductive data was taken. It was hoped to repeat these measurements of the photoconductivity for the CC1 sample, where the charge density and temperature could be varied independently, but due to the failure of the contacts to the back gate right before the lab shut down for renovations, these measurements could not be made.

The qualitative agreement between this model and the photoconductive data indicate that heating of the electron gas is the dominant detection mechanism for our devices. The of-order-microsecond photosignal decay times observed are consistent with electron heating as well. That the peak of the photoconductive response occurs around 20K for the DSQB sample means that detector systems implementing this detection mechanism could use cooling systems without liquid cryogens, such as hydrogen sorption coolers.[30, 8] Launching and flying satellites with dewars of liquid helium adds weight, expense, and complexity to space missions, as well as the fact that the mission duration is limited by the cryogens. For all of these reasons, there is great interest in developing THz detectors that could be operated

without liquid cryogens, to significantly increase the amount of science attainable per project cost. These photoconductive measurements demonstrate that electron heating effects in semiconductor quantum well heterostructures can operate well in the required temperature range, and so are good candidates for further investigation. The next phase is to make devices with improved sensitivity. The devices described in this dissertation were made very large, to allow the capacitance to be measured easily for diagnostic purposes. By significantly reducing the size of the detectors and using more efficient optical coupling techniques, the sensitivity will be increased. With these two improvements, a given quantity of THz radiation will be coupled to, and absorbed by, a smaller number of electrons, leading to much larger changes in the device output. Work is underway to make a new generation of antenna-coupled devices, with an improved antenna structure, and with an active region of order $10\mu m^2$.

With a better understanding of the processes that combine to give the observed temperature dependencies of the energy relaxation time and electron mobility, it should be possible to engineer the optimal operating temperature of these detectors. Simultaneous measurements of gate photovoltage and absorption can yield the intersubband population relaxation time. In this work, the energy and population relaxation times are treated in the models as if they were the same. In the general case, the two relaxation times can be different. However, in these samples, this simplifying treatment should be reasonable. This issue will be discussed in further detail in the next chapter. The simultaneous gate photovoltage and absorption measurements were performed on the CC1 sample, where the presence of a back gate as well as a front gate, allows the electric field across the well and the charge density to be varied independently, and each independently of the temperature. In this system, much can be learned about the behavior of the intersubband population relaxation time.

Chapter 7

Gate Photovoltage Results

The gate photovoltage measurements looked at the change in voltage between the front gate and the channel quantum well induced by the THz light. The front gate and channel quantum well form a parallel-plate capacitor. The channel was grounded, and a DC voltage was applied to a resistor in series with the front gate. The voltages at the gate and quantum well were sent to a differential preamplifier. The front and back gate voltages were varied, changing the electric field and charge density in the quantum well, in order to tune the intersubband transition through the fixed FEL frequency (103cm^{-1}.) Figure 7.1 shows that the gate photovoltage signal and transmission both tune through the intersubband transition resonance in the same way.

The photovoltage was generated both by a change in the capacitance and a change in the chemical potential of the illuminated electron gas. When the THz light was absorbed, the average position, in the heterostructure growth direction, of the electron gas changed due to the different spatial distribution of the two subbands wavefunctions. This displacement changed the effective separation between the two plates of the capacitor, changing the gate-well capacitance. The absorbed THz light also added energy to the electron gas, changing the electron temperature. The chemical potential of the illuminated region of the electron gas changed with the rise in

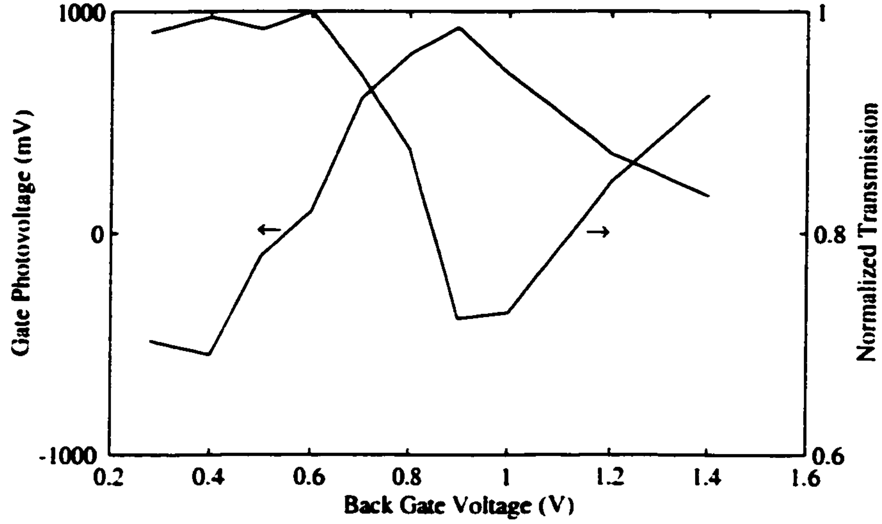

Figure 7.1: Gate photovoltage peak signal and relative transmission for the CC1 sample, tuning through the intersubband transition. FEL frequency is 103cm^{-1}.

temperature.

The two expected effects, from the change in capacitance and from the change in chemical potential, can be combined. In the circuit model, shown in Figure 7, at time $t = 0$, the capacitance jumps from $C \rightarrow C' \equiv (C + \Delta C$ and the battery V_μ is switched in. The gate photovoltage measured corresponds to the change in the voltage difference $V_{FG} - V_{GND}$, due to the onset of illumination. The photovoltage should be considered relative to V_{GND} rather than V_{Ch} because the electrical leads to the device make contact with a pool of unilluminated electrons that do not heat up. Thus the local potential at the leads, that is sensed by the amplifier or oscilloscope, is that of ground, and not the region of changing chemical potential.

For this circuit model, the voltage equation can be written, for time $t > 0$,

$$V_{Bat} = \dot{Q}R + Q/C' + V_\mu \tag{7.0.2}$$

Defining an effective voltage, $V_{eff} \equiv V_{Bat} - V_\mu$,

$$(RC')\,\dot{Q} + Q - C'V_{eff} \tag{7.0.3}$$

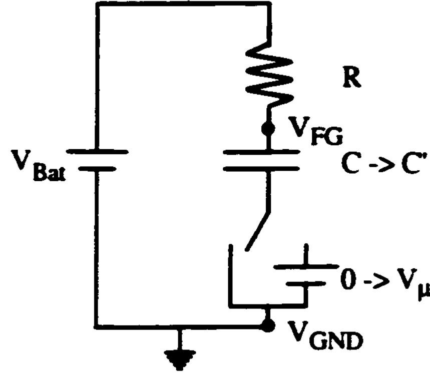

Figure 7.2: Circuit model combining the effects of the photo-induced changes in capacitance and chemical potential. At time $t = 0$, the capacitance changes from $C \to C'$ and the battery V_μ is switched into the circuit. V_{FG} and V_{Ch} are the voltages at the front gate and the channel quantum well contacts.

which is solved by a function of the form

$$\begin{aligned} Q(t) &= Ae^{-t/RC'} + B, \\ &\text{subject to the conditions} \\ Q(t=0) &= CV_{Bat} \\ Q(T \to \infty) &= C'V_{eff} \end{aligned} \tag{7.0.4}$$

to give the solution for the charge on the capacitor,

$$\begin{aligned} Q(t>0) &= \left[CV_{Bat} - C'V_{eff}\right] e^{-t/RC'} + C'V_{eff} \\ &= \left[-\Delta CV_{Bat} + (C+\Delta C)V_\mu\right] e^{-t/RC'} + (C+\Delta C)(V_{Bat} - V_\mu) \end{aligned} \tag{7.0.5}$$

By convention, V_{GND} has the same value at all times, so the modeled gate photovoltage, V_{PV} can be expressed,

$$\begin{aligned} V_{PV}(t) &= \Delta(V_{FG} - V_{GND}) \\ &= V_{FG}(t>0) - V_{FG}(t<0) \\ &= \left[V_{Bat} + (\tfrac{C}{C'}V_{Bat} - V_{eff})\, e^{-t/RC'}\right] - V_{Bat} \\ &= (\tfrac{-\Delta C}{C'}V_{Bat} + V_\mu)\, e^{-t/RC'} \\ &\approx (\tfrac{-\Delta C}{C'}V_{Bat} + V_\mu) \end{aligned} \tag{7.0.6}$$

The timescales of the measurements are all much smaller than the RC' time constant, so the exponential factor is nearly unity. In particular, for the measurements on CC1,

Sample	CC1	DSQB
V_{Bat}	negative	negative
C'	positive	positive
ΔC	positive	negative
$\frac{-\Delta C}{C'} V_{Bat}$	negative	positive
$V_{\mu} = \Delta\mu / -\lvert e \rvert$	positive	positive

Table 7.1: Polarity of the terms in Equation 7.0.6 for the gate photovoltage modeled for samples CC1 and DSQB. The last two rows show that the two effects are expected to be in opposition for the CC1 sample but to be additive for the DSQB sample.

$RC' \approx 300\mu s$, and the FEL pulse length used, $3.7\mu s$. The exponential would have dropped to only 98.7% when the FEL pulse ended. The system would then relax with a combination of time constants, the FEL fall time (approximately $1\mu s$), and the population relaxation time for the capacitance and the energy relaxation time for the chemical potential.

For both the DSQB sample and the CC1 sample, a negative voltage was applied to the front gate for all measurements. When electrons in the active region of the quantum well absorbed the THz photons, exciting them to the upper subband their average position changed. For the DSQB sample, the electrons shifted towards the narrow well, which is farther from the surface, as shown in Figure 3 on page 19. For the CC1 sample, the front gate was generally at a negative voltage with respect to the back gate, and this applied electric field caused the population of excited electrons to be nearer to the surface. Thus, the displacements for the two samples are opposite. On the other hand, for both samples, the absorbed energy would cause the temperature of the electrons to rise, causing the chemical potential to decrease. As outlined in Table 7.1, the two effects are expected to be in opposition for the CC1 sample, and of the same polarity for the DSQB sample.

7.1 Polarization

When the electrons in the channel quantum well absorb the THz photons, they are excited to the upper subband, which has a different wavefunction spatial distribution than the ground subband. The change in the expectation value of the electrons' position leads to the change in capacitance discussed in the circuit model above. However, the electron displacement can also be thought of as a absorption-induced dipole. The electron-displacement contribution to the gate photovoltage, V_P, is more easily calculated in terms of the polarization, P, than of the expectation value and capacitance. The expression of the voltage contribution from the polarization, in CGS units, is,

$$\Delta V_P = \frac{4\pi}{\varepsilon} P \tag{7.1.1}$$

In James Heyman's gate photovoltage and absorption experiments on another piece of the DSQB wafer, the intersubband population relaxation times were investigated for independently-varied temperature and incident THz intensity.[17] The experiment and sample design were similar to those used for the samples discussed in this dissertation. Also, similar to both experiments, Heyman used the gate voltage to tune the intersubband resonance through the fixed FEL frequency. The temperature dependence was investigated at a low incident THz power, in the regime where the photovoltage was linearly dependent on intensity. A lifetime of 1.2 ns was found for 10K, with the lifetime strongly dependent on temperature, dropping to 6 ps at 50K. This activation energy of this temperature dependence is consistent with the emission of longitudinal optical (LO) phonons becoming the primary relaxation mechanism as the temperature increases. Above 50K, qualitatively a similar trend is observed that may be consistent with increasing LO phonon emission, but the lineshape of the photovoltage peaks changes, that Heyman speculates may be due to thermionic emission and photothermal excitation between the well and doping regions. At a single temperature, 10K, the THz intensity was varied. At low-intensities, the photovoltage is linear in intensity, and the intersubband relax-

ation time of 1.2 ns was determined. The time constant changes dramatically with intensity dropping to 15ps at the strongly-saturated intensity of 2 kW/cm^2. Heyman suggests that at the high intensities, electron-electron intersubband scattering, which depends strongly on the population in the upper subband, will have a large effect. Also, at high intensities, the temperature of the electron gas will be elevated, so the temperature-dependent relaxation mechanisms, such as LO phonon emission, will be operating. In this work the chemical potential was not considered, although its effect should also be present.

Following Reference [17], the polarization can be calculated by perturbation theory for the susceptibility in equilibrium, to yield, also in CGS units,

$$P = -|e|\,(z_{2,2} - z_{1,1})\,(\Delta n^o_{1,2})\,\frac{I\sigma T_{pol}}{\hbar\omega}\left(1 + 2\frac{I\sigma T_{pop}}{\hbar\omega}\right)^{-1} \qquad (7.1.2)$$

where $(z_{2,2} - z_{1,1})$ is the difference in position matrix elements for the two subbands, $\Delta n^o_{1,2}$ is the equilibrium population difference between the two subbands. σ is the linear absorption cross-section, $\sigma(\omega)$, of an electron in a quantum well with only two-subbands with the depolarization-shifted resonance frequency $\tilde{\omega}_{1,2}$ but which is excited with the frequency ω. T_{pop} is the subband population relaxation time constant. I is the incident intensity. This equation is valid for all intensities from the low-power linear regime through saturation. All of these quantities are available, save T_{pop} that is to be solved for, from data or from a self-consistent calculation of Poisson's and Schrödinger's equations for the quantum well. However, another measured quantity, the absorption coefficient, is also derived from the dielectric constant or susceptibility and can make this equation much simpler.

As a convention, in this dissertation, voltages may be positive or negative, but I will always express the charge of an electron as —e—. This unusual notation is chosen to make clear the sign and polarity of all the equations and quantities discussed.

The absorption coefficient, α, is a measure of the strength of the absorption per unit length along the direction of propagation of the incident light. The position-

dependent intensity is then given by the exponential,

$$I(x) = I_o e^{-\alpha x} \tag{7.1.3}$$

With the theory used to calculate the polarization, the absorption coefficient is given by,

$$\alpha(I) = (\Delta n^o_{1,2}) \frac{\sigma}{a} \left(1 + 2\frac{I\sigma T_{pol}}{\hbar\omega} \right)^{-1} \tag{7.1.4}$$

with the only additional factor being a, the thickness of the sample wafer. Substituting this expression in Equation 7.1.2 gives a much simpler expression for the polarization, with far fewer model-derived parameters,

$$P = -|e|(z_{2,2} - z_{1,1}) \frac{\alpha a I}{\hbar\omega} T_{pop} \tag{7.1.5}$$

The absorption coefficient is determined from the optical transmission measured simultaneously with the gate photovoltage. The absorption of the electrons was found by comparing the transmission of the sample under normal operating gate voltages, with charge in the well, to the transmission through the sample when the well was depleted of mobile charge. The procedure I used to normalize the transmission data for the back-gated samples is as follows. First the transmitted intensity was divided by the simultaneously-collected signal from the reference detector (see Figure 5.4 for the optical layout of the experiment) to normalize out the shot-to-shot intensity fluctuations of the FEL pulses. Then I took the ratio of the normalized transmission at each pair of gate voltages with the maximum normalized transmission from all the gate voltages. From Equation 7.1.3 the absorption coefficient is derived from the measurements by,

$$\alpha(V_{FG}, V_{BG}) = \frac{-1}{L} \ln \left(\frac{I_{trans}(V_{FG}, V_{BG})}{I_{maxtrans}} \right) \tag{7.1.6}$$

where V_{FG} and V_{BG} are the front and back gate voltages at the measurement was taken, and L is the length of the sample. There is some absorption by non-mobile charge trapped in the well when the well is nominally depleted, but I took data at a set of gate voltages that not only depleted the well, but also applied an electric field

well away from that for resonant absorption. In this manner I tried to minimize the effect of the non-mobile charge on the absorption coefficient.

7.2 Chemical Potential

The chemical potential contribution to the gate photovoltage comes from the heating of the electron gas and the temperature dependence of the chemical potential. The timescales of these measurements are much shorter than the RC time constant, and the effect of the change in chemical potential is to shift the potential of the hot electron gas by the voltage V_μ.

$$V_\mu = \frac{\mu(T_e) - \mu(T_L)}{-|e|} \tag{7.2.1}$$

where T_L is the temperature of the lattice and of the cold, unilluminated electrons, and T_e is the temperature of the illuminated electrons gas. The differential preamplifier or oscilloscope are connected across the front gate and the channel quantum well, but the electron gas near the ohmic contacts to the well are not illuminated and so stay cold. The voltage seen by the preamplifier is $V_{FG} - V_{GND}$, shown in Figure 7.

A photovoltage due to the temperature-dependent chemical potential was reported by Batke, Kaminski, Kotthaus, and Spector in 1989.[6] Their experimental circuit, with a resistor in series with the capacitive device, was similar to mine, even to using UCSB's Free Electron Lasers as the THz source. Their sample was a GaAs/AlGaAs heterojunction, with grating gate, which is used to couple the THz light to the sample. The grating gate was used change the charge density at the heterojunction, and so tune the plasmon modes of the quantum well through the fixed FEL frequency. On resonance, the electron gas heats up, changing the chemical potential, which yields a voltage difference between the gate and the electron gas at the interface. In their experiments, significant photovoltage was observed with the polarization of the THz light perpendicular to the lines of the grating, and

no response for the parallel polarization, as expected for grating-coupling the THz light into the device. The gate photovoltage showed two features with changing gate voltage. A negative photovoltage peak was observed at the gate voltage corresponding to a plasmon resonance. Another peak was observed at a more negative gate voltage, corresponding to the tail of a broad 1D intersubband resonance where the quantum well under the gate stripes was fully depleted, to leave 1-D wires with electrons. There is also a positive background photovoltage for gate voltages below that of the plasmon resonance. Batke and colleagues qualitatively explain the sign of the plasmon-resonant photovoltage by the temperature-dependent chemical potential, but they do not present any quantitative discussion, other than indicating that the observed photosignal represents a self-consistent rearrangement of the interface potential with the THz absorption.

The temperature dependence of the chemical potential comes from the Fermi-Dirac distribution of states, $f(E,\mu,T)$, where the distribution extends infinitely to higher energies, but is bounded by the minimum energy of the lowest energy state.

$$N_s = \int_0^E \rho(E) f(E,\mu,T) dE = \int_0^E \rho(E) \frac{1}{1 + e^{(E-\mu)/K_B T}} dE \qquad (7.2.2)$$

$\rho(E)$ is the density of states at an energy E. The temperature dependence of the chemical potential can be determined by the following expression for the charge density, assumed constant with temperature, in a quantum well with exactly two subbands[13].

$$N_s = \frac{m^* K_B T}{\pi \hbar^2} \sum_j \ln\left(1 + e^{\frac{-(E_j - \mu(T))}{K_B T}}\right) \qquad (7.2.3)$$

where the E_j are the energies of the bottoms of the subbands. At zero temperature, this equation is a definition of the Fermi energy, $E_F = \mu(T=0)$. The chemical potential at non-zero temperatures is often also called the Fermi energy, but this terminology is imprecise and is avoided here for clarity of discussion.

The chemical potential can be calculated analytically for this two-subband sys-

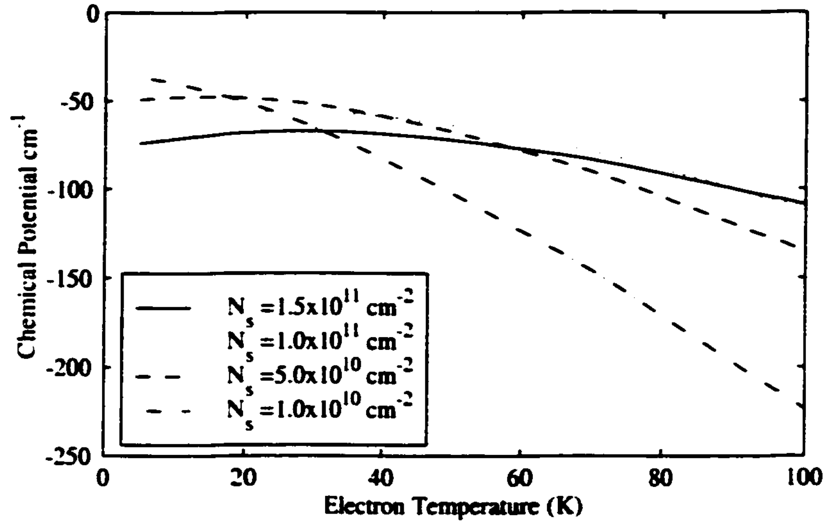

Figure 7.3: Chemical potential as a function of temperature for several charge densities, all at an electric field of -0.1V. The difference between the chemical potential at warmer temperatures and at 10K is, in general, negative. However, for the highest charge densities, where the chemical potential is close to the bottom of the second subband, the chemical potential can actually increase with temperature.

tem. Following Reference [13], and making the following substitutions,

$$\begin{aligned} r &= \exp\left(\frac{\pi\hbar^2 N_s}{m^* K_B T}\right) \\ s_1 &= \exp\left(\frac{-E_1}{K_B T}\right) \\ s_2 &= \exp\left(\frac{-E_2}{K_B T}\right) \\ u &= \exp\left(\frac{\mu}{K_B T}\right) \end{aligned} \tag{7.2.4}$$

then Equation 7.2.3 can be transformed into the following form,

$$r = \prod_j (1 + s_j u) \tag{7.2.5}$$

which is just a quadratic equation. Solving then for the chemical potential gives,

$$\mu(T) = K_B T \ln\left[\frac{s_1 + s_2}{s_1 s_2}\left(-1 + \sqrt{1 - 4(1-r)\frac{s_1 s_2}{(s_1 + s_2)^2}}\right)\right] \tag{7.2.6}$$

The steady-state electron temperature for the illuminated electron gas is approximately given by the lattice temperature and the change in temperature due to the

power absorbed within the energy relaxation time T_{eng}.

$$T_e = T_L + \frac{P_{abs} T_{eng}}{C_v(T_L)} \tag{7.2.7}$$

Putting everything together, this model can be used to extract a relaxation time for each pair of front and back gate voltages. The model equations combine to form a nonlinear equation with only one unknown, the relaxation time, and one photovoltage measurement. All the other parameters in the model can be taken from data or from a simultaneous solution of Schrödinger's and Poisson's equations for the quantum well structure. Thus this nonlinear equation can be solved to unambiguously extract a relaxation time for each pair of gate voltages independently.

7.3 Comparing Model to Data

The polarization and chemical potential effects can be combined to explain features in the data, but neither effect on its own is even qualitatively correct. Figures 7.4 and 7.5 show the actual gate photovoltage data and the values calculated from the model for the solutions to the relaxation time nonlinear equation. For comparison, Figures 7.6 and 7.7 show the contributions from the two effects that are added together in the model.

Qualitatively, neither effect alone can explain the large regions of both positive and negative photovoltage. The polarity of the polarization is set by the matrix element $z_{22} - z_{11}$, which only switches signs, for this square well, when the applied electric field switches polarity. Since the gate photovoltage switches signs while the electric field remains negative in these experiments, this effect cannot explain the observed positive and negative photovoltage. The chemical potential in general decreases with increased electron temperature. The only regime in which it increases for this quantum well system is when the charge density is large enough that the unilluminated chemical potential is close to the bottom of the upper subband. In that case, with rising temperature, the chemical potential can rise into the second

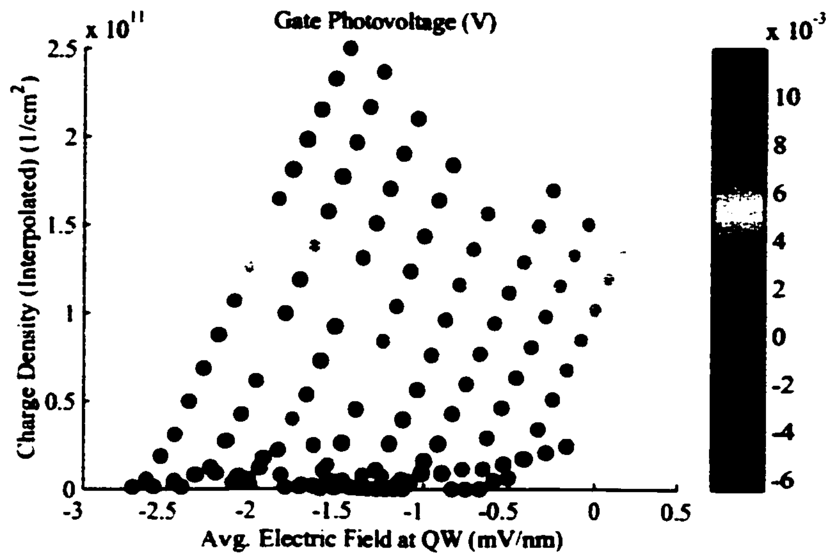

Figure 7.4: Gate photovoltage data, at 10K.

subband where suddenly there are more empty states available to the electrons. This effect is shown in Figure 7.3. The only region of parameter space that the chemical potential effect could give a negative photovoltage for this sample would be at large charge densities, just before the second subband starts to be filled. Thus this effect also cannot explain the observed positive and negative photovoltage.

Another feature that requires both effects to be explained is the shift of the maximum photovoltage away from the peak absorption. This shift towards lower charge densities can be seen by comparing Figures 7.4 and 7.3. Both the polarization effect and the chemical potential effect independently have their maximum magnitude where the absorption is strongest. This makes sense, as both effects are due to the absorbed light. Thus, no matter what time constants were used, neither effect alone can explain the shift of the region maximum signal.

The two components in the model presented here have each been independently reported for similar experiments in the literature, the polarization by Heyman and chemical potential effects by Batke. In these two experiments, only one effect was considered, but both should be present according to my model. For Heyman's exper-

iment, in order to explain all of his results, the polarization effect must be dominant in the DSQB samples. However, as noted in Table 7.1, both effects would contribute in the same way to the measured gate photovoltage, so there would not have been any effects as obvious as the dual polarities observed in my sample to announce the presence of a second effect. This model would be consistent with his measurements so long as the chemical potential effect was small for his experimental parameters. For Heyman's low-power experiments, the electron temperature is not expected to rise much above the lattice temperature, both on phenomenological grounds and also from the calculation by Murdin in Reference [33]. For Batke's experiment, the polarization of the incident THz light was in the plane of the quantum well, and this polarization will not couple to the intersubband transition. However, the electron gas was heated, and so there would be a thermal re-distribution of electrons between the two subbands, so both effects could still be present. In Batke's experiment, the AlGaAs layer was grown on top of a GaAs substrate, so the electrons in the upper subband would have a average position farther from the surface than the ground subband. Thus, as in Heyman's experiment, the polarization effect would contribute positively to the gate photovoltage. It is not apparent from their paper if their electrical contact to the inversion charge layer contacted a illuminated (hot) or unilluminated (cold) region of the electron gas, in which case the photovoltage contributed by the change in chemical potential would be negative or positive, respectively. Their data shows a negative gate photovoltage, so I assume that the polarization effect (positive) would reduce the magnitude of their observed photovoltage peak. In either case, they do not present any quantitative analysis of the peak height. The positive polarization effect may help explain the positive background that they observed off-resonance.

7.4 Relaxation Times

The relaxation time can be extracted for every pair of front and back gate voltages by a solution of the model equations, forming a nonlinear equation in the relaxation time. The results are shown in Figure 7.9. Each point is an independent numerical solution to the model nonlinear equation with parameters appropriate for that point in gate voltage space, an equation with one unknown to be solved for and one data value. Trends in the relaxation time can be investigated independently for charge density and electric field, and each independent of the temperature. Given the sometimes unpredictable results from numerically solving nonlinear equations, and the fact that there has been no smoothing or attempt to reduce the noise from any of the measurements that went into the parameters of the equation, the smoothness of the resulting solutions is somewhat remarkable. It should be noted, however, that for 34 of the 141 data points in this set of data, the nonlinear equation did not have a solution or the solving algorithm did not converge. These points are all in the same region of parameter space; all have charge densities below approximately $5x10^{10}cm^{-2}$. This issue is discussed below.

The parameters in the model nonlinear equation all come from data or from modeling. The z_{ij} matrix elements and subband energies came from a modeling program written by Bryan Galdrikian, that simultaneously solves Schrödinger's and Poisson's equations for the quantum well structure. This program has been used with good agreement to data for numerous structures designed in this research group over the last decade. All the rest of the parameters are derived from measurement.

The relaxation time constants extracted for charge densities above $5x10^{10}cm^{-2}$ are of order nanoseconds, ranging from 5ns to around 0.1ns at lower charge densities. These times are consistent with James Heyman's results for low incident intensities and low temperatures, discussed in Reference [17], where he found a subband population relaxation time of 1ns at 10K. The energy relaxation times reported by Murdin in Reference [33] for moderately wide GaAs/AlGaAs wells were

200-500ps, also reasonably consistent with the times found here.

Several general trends can be seen in the extracted relaxation times. The time constants decrease with decreasing charge density, but do not exhibit a strong dependence on electric fields applied across the well. There is a decrease in the time constants in the region of resonant absorption, however.

The extracted relaxation time decreases with decreasing charge density, for charge densities above $5x10^{10}cm^{-2}$ where the model nonlinear equation is solvable. Qualitatively this trend is consistent with Pauli blocking. At large charge densities there are fewer unoccupied low-energy states for energetic electrons to scatter into, via longitudinal-optical (LO) phonon emission or other processes. The reduced availability of appropriate final states for scattering suppresses energy and subband population relaxation. At lower charge densities, this suppression is reduced, so the relaxation times decrease. The lack of a strong change in the relaxation times at high fields, where the electrons are closest to the well barriers, reconfirms that such scattering processes as interface roughness scattering or remote impurity scattering are not important for energy or population relaxation.

There is a trend of decreased relaxation times in the region of parameter space near resonant absorption. The base-10 log of the relaxation time is -9.0 to -9.6 in the region of resonant absorption, and -8.0 to -8.5 in the surrounding region. The incident intensity was constant over the entire data set, eliminating intensity-dependent explanations. The origin of this order-of-magnitude decrease in the relaxation time may be related to the electron temperature. If the electrons were heated to elevated electron temperatures above the longitudinal optical (LO) phonon bottleneck[33], then the energy relaxation time would be expected to decrease due to increased emission of LO phonons by the most energetic electrons in the tail of the Fermi distribution. The electron temperatures in the region of resonant absorption calculated from the model were larger relative to the temperatures farther away, but the magnitudes of the temperatures are unphysically large, so this qualitative trend cannot be taken as definitive.

7.5 Problems with the Model

There are two fundamental breakdowns of this model that should be addressed. The first is the divergence of the nonlinear equation for low charge densities, and the other is the unreasonably large electron temperatures that the model yields.

For 35 of the 141 data points in this data set, the nonlinear equation solver algorithm used diverges. For 33 of these points, the nonlinear equation does not have a real (non-complex) solution; the minimum calculate photovoltage for any non-infinite time constant is still larger than the actual data. These problem points all occur at low charge densities, below around $5x10^{-10}cm^{-2}$ with most below $1x10^{-10}cm^{-2}$. If anywhere, it is to be expected that the model would break down at low charge densities, since the data was collected at gate voltages extending well into the depleted regime. The physics of isolated puddles of numbers of electrons is very different than the well-behaved Fermi sea assumed in many aspects of the theory presented here. The threshold above which the integrated charge density rises above the noise in the capacitance-voltage curves is around $1x10^{9}\mathrm{cm}^{-2}$. The comparatively large charge densities for which there are no real solutions are thus surprising.

The other major breakdown of the model is the unreasonably large electron temperatures that correspond to the extracted relaxation times. The electron temperatures range from 100K at low charge densities to 800K at the higher charge densities. These temperatures are simply unphysically large. The theory for each of the two effects is well documented, the polarization by Heyman's experiments, and the chemical potential from fairly simple theory. It is hypothesized that the large electron temperatures are due to the mathematical fragility of the model. The crossover from negative to positive photovoltage happens in the region of resonant absorption. Thus for many points, the magnitude of the two calculated contributions to the photosignal using the extracted time constants, shown in Figures 7.6 and 7.7 are much larger than the size of the data. Fitting a small value with the difference of two much

larger numbers is not mathematically robust. In that case, then the model nonlinear equation could be sensitive to small changes in the input parameters. This fragility could account for the unreasonably large electron temperatures yielded by solutions to this model, even though all the input parameters are derived from experiment and well-tested simulation. Of the input parameters, the power incident on the sample has the largest error bounds, +21%,-17%, due to the series of measurements that are combined in the intensity calibration, as explained in Appendix A. As mentioned in the appendix, coupling of the THz radiation from free-space propogation to waveguide modes inside the sample was ignored in the intensity calibration due to a lack of the complex calculations necessary to quantify it. The error of ignoring the coupling effects may also contribute to the problems of the nonlinear equation solutions.

Mathematical fragility of the nonlinear equation may make the model sensitive to the assumptions involved in the theory. One assumption that should be considered is the use of a single time constant for both the energy relaxation and subband population relaxation is incorrect.

Energy relaxation and subband population within a quantum well are, in general, distinct, and either can be larger than the other. Longitudinal optical (LO) and acoustic phonons are the dominant mechanisms in energy and population relaxation in these quantum well structures. The subband energy spacing in these wide well structures is below the minimum energy to emit a LO phonon, so at most only a small fraction of the electrons can emit LO phonons. Thermalization of the electron energies occurs on very fast timescales, of order 1ps, however, through electron-electron scattering and ionized impurity scattering. The timescales for these and other processes are summarized and discussed in Murdin's paper, Reference [33]. Electron-electron scattering will be a weaker process at the lower charge densities, but ionized impurity scattering would still be available. The energy and subband population relaxation processes are slower, such that it is entirely appropriate to describe the energy distribution of the electrons in the quantum wells studied by a single electron temperature. Murdin and colleagues present data demonstrating a

LO phonon bottleneck. At temperatures below the bottleneck, the energy relaxation rate is limited by acoustic phonon emission. Only above this crossover temperature do enough of the thermalized electrons have sufficient energy to emit a LO phonon for this very fast, sub-picosecond, process to become the rate-limiting process in energy relaxation.

The powers used in these experiments were attenuated to be in the regime where the photovoltage changes linearly with intensity. In this regime, the electron temperature is not expected to be far above the lattice temperature, which was 10K for the data presented here. The sample is probably then operating below or around the LO phonon bottleneck. In either case, the thermalization time would be much faster, by perhaps as much as two orders of magnitude (of order 1 ps, while Murdin determined energy relaxation times rate-limited by acoustic phonon emission to be around 500 ps for wide quantum wells.) Although the energy and subband population relaxation times may be different, the rapid thermalization is expected to constrain the two times to be of similar magnitude.

7.6 Detector Responsivity

The responsivity of these devices can be calculated directly, using the measurements of the photovoltage and the reference measurement of the FEL power. The responsivity of a detector is the ratio of the detector output to the incident power. The reference measurement of the FEL power is accomplished by splitting off a portion of the FEL beam and measuring its power, as shown in the schematic in Figure 5.4. In this manner pulse to pulse fluctuations in the FEL power can be monitored. The reference power was calibrated to the power of the beam at the position of the sample. All of the calibration measurements, calculations, and error are described in Appendix A. The transmission of the cryostat windows and the black polyethylene optical filter were measured with Fourier transform infrared (FTIR) spectroscopy. With these transmission factors, and a geometric factor for the portion of the beam

intersected by the sample aperture, the power incident on the sample can also be calculated. This incident power is the power in the portion of the beam just outside the sample. The power just inside the sample is the incident power multiplied by the transmission of the GaAs/He gas interface (the sample was in a helium flow cryostat.) All effects of coupling to waveguide modes have been ignored for simplicity.

With the calibrated FEL power incident on the sample, the highest responsivity values, of both polarities, for the photovoltage detection mode of the CC1 sample are,

$$\begin{aligned} \mathcal{R}_{pos} &= 0.13V/W \quad +21\% - 17\% \\ \mathcal{R}_{neg} &= -0.070V/W \quad +17\% - 21\% \end{aligned} \tag{7.6.1}$$

This device was not designed to test the ultimate sensitivity of detection, but rather to be large enough to have an easily-measured capacitance for diagnostic purposes. In order to be able to compare this value to other detectors, the responsivity scaled by the area of the illuminated active region may be useful. The scaled responsivities are then, approximately, $8x10^5 V \mu x^2/W$ and $4x10^5 V \mu x^2/W$.

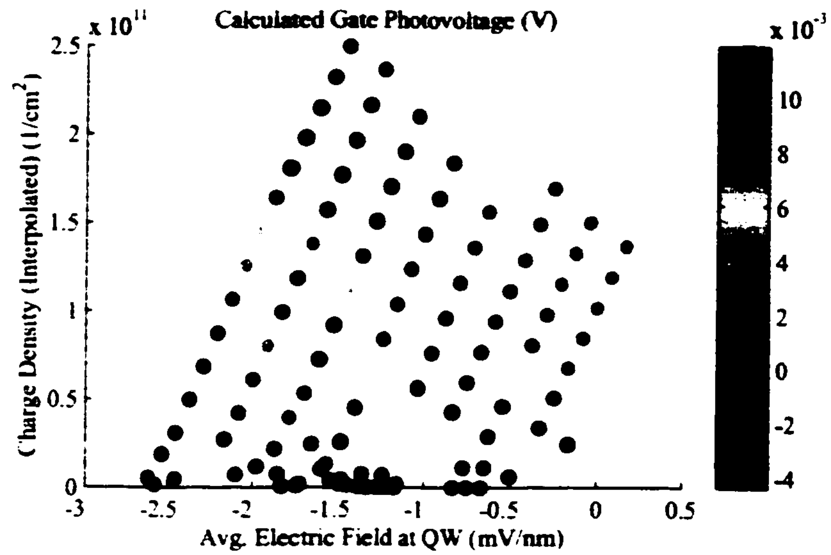

Figure 7.5: Calculated values for the gate photovoltage using the extracted relaxation times.

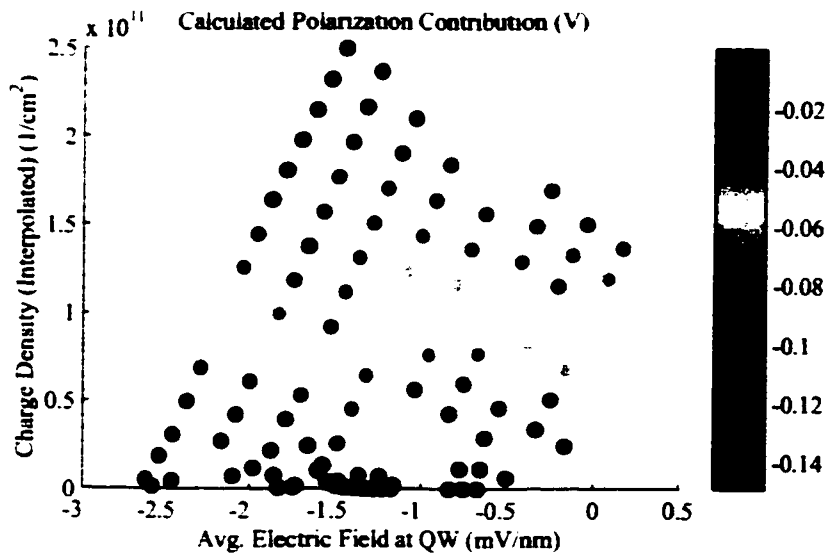

Figure 7.6: Calculated contribution to the photovoltage from the polarization effect, using the extracted relaxation times.

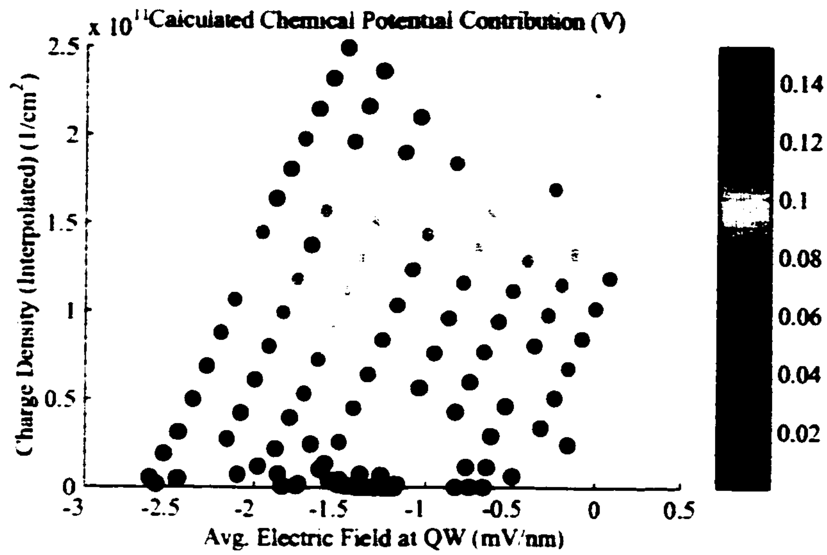

Figure 7.7: Calculated contribution to the photovoltage from the chemical effect, using the extracted relaxation times.

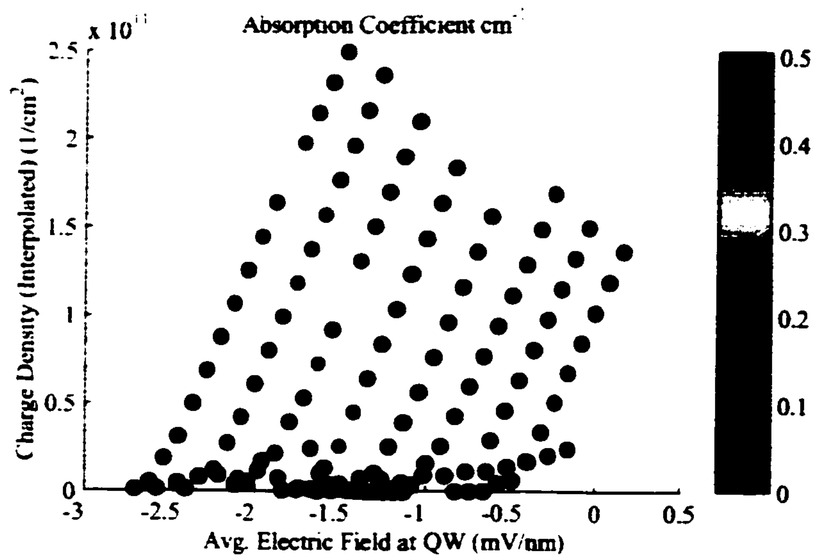

Figure 7.8: Absorption coefficient, in cm^{-1}

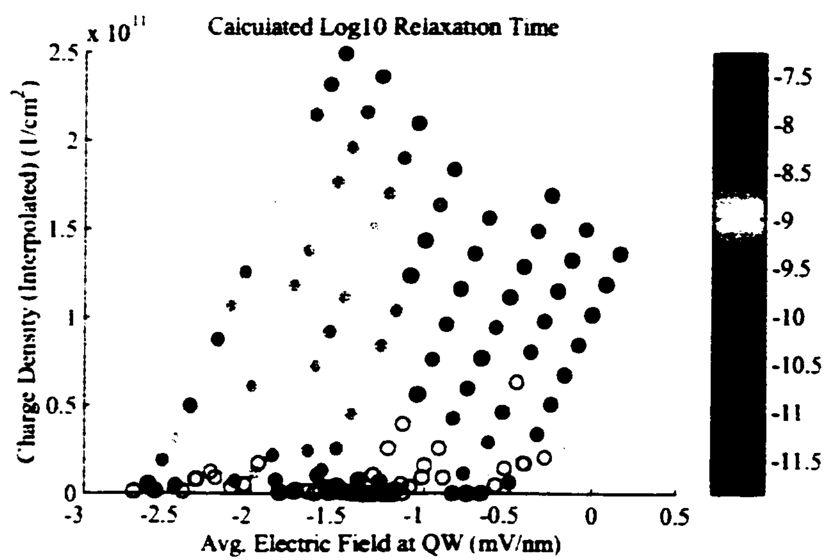

Figure 7.9: Relaxation times extracted from the combined model. Open circles are the points for which the model equation had no solution.

Chapter 8

Conclusion

A new kind of far infrared detector has been made using intersubband transitions in GaAs/AlGaAs quantum well heterostructures. With these detectors, from two different quantum well structures, detection of THz light has been demonstrated by both in-plane photoconductivity and gate photovoltage. Both detection modes operate at relatively warm temperatures. Photoconductive signal was observed for a double asymmetric quantum well from 5K to around 75K, with the maximum signal at 20K. The usability of these physical processes for detection at these temperatures offers the possibility that future iterations of these detectors could be used in space missions without needing liquid cryogens.

The current generation of devices has been designed to accommodate several diagnostic measurements that allow the detection mechanisms and intersubband dynamics to be studied. Electrical and optical measurements were carried out, including current-voltage curves, capacitance-voltage curves, and optical transmission simultaneous with photoconductivity or gate photovoltage. These measurements were carried out over a range of front, and where applicable, back gate voltages to span both electric field across the well and charge density. The optical measurements were with UCSB's free electron laser (FEL), attenuated into the low-power regime where the photoresponse was linear with intensity.

In the photoconductive detection mode, the absorbed THz light heats up the electron gas, and this change in temperature is detected as a change in the in-plane resistance. The temperature dependence of the maximum photoresponse for the asymmetric double quantum well is qualitatively explained by a bolometric model, characterized by a product of the energy relaxation time and the relative change in electron mobility. When estimates of all the other parameters needed to calculate the expected photoresponse, the model predictions are around the same order of magnitude as the data. Since the intensity was not calibrated for these measurements, more quantitative analysis and figures of merit cannot be given.

In the photovoltage detection mode, the observed photosignal for a wide quantum well was both positive and negative for different ranges of charge density and applied electric field. The presence of both polarities was not initially expected, and requires contributions from two physical processes in order to be even qualitatively explained. The polarization contribution to the gate photovoltage arises from the net displacement of the electron gas when electrons absorb THz photons and are excited to the upper subband. The chemical potential contribution to the photovoltage comes from the change in electron temperature of the excited electron gas and the temperature dependence of the chemical potential. A simple circuit model was devised to combine these two effects. With this model, the relaxation time for each pair of gate voltages can be determined independently as the solution to a nonlinear equation, where all other parameters are taken from measurement or from a self-consistent model of the quantum well heterostructure. In this manner, the dependence of the relaxation time on electric field and charge density can be determined independently, and also independently of the temperature.

The model qualitatively explains the presence of both photovoltage polarities for the wide well CC1 but only positive photovoltage for the DSQB double quantum well. It also can account for the shift in maximum photovoltage to lower charge densities than the region of resonant absorption. Quantitatively the model breaks down in that the nonlinear equation for the single relaxation time does not have so-

lutions for many points with low charge density and in that the electron temperatures corresponding to the extracted time constants are unreasonably high. With the extracted times, the calculated photovoltage is a small difference between two much larger values, which is mathematically not robust. Probably the model equation is sensitive to modest variation of one or more parameters. The parameter with the largest uncertainty is that of the absorbed power, through uncertainties in the intensity calibration. Efforts are currently underway to try to understand how uncertainty in the absorbed power or other parameters affects the model calculations.

These detectors were not intended to test the ultimate sensitivity achievable with these mechanisms, but the devices do demonstrate that the relevant physical phenomena can be implemented and used in detectors at temperatures well above 4K. This project is being continued in the research group, and fabrication of next generation of detectors has begun. These new detectors will return to having a small active regions, of order $30\mu m^2$, for increased sensitivity. An antenna and filter circuit are being incorporated for better optical coupling and to test these detection mechanisms in a heterodyne mode. Insight gained from the diagnostic devices presented here will continue to be applied to future iterations of detectors in this ongoing project.

Bibliography

[1] *Proceedings of the Far-IR, Sub-mm & MM Detector Technology Workshop, April 1-3 2002, Monterey CA*, 2002. In press.

[2] T. Ando, A.B. Fowler, and F. Stern. Electronic properties of two-dimensional systems. *Reviews of Modern Physics*, 54(2):437–672, April 1982.

[3] N.G. Asmar, J. Cerne, A.G. Markelz, E.G. Gwinn, M.S. Sherwin, K.L. Campman, and A.C. Gossard. Temperature of quasi-two-dimensional electron gases under steady-state terahertz drive. *Applied Physics Letters*, 68(6):829–31, February 1996.

[4] M. Baes and H. Dejonghe. Dark matter halos around elliptical galaxies: how reliable is the stellar kinematical evidence?. *Astrophysical Journal, Letters*, 563(1):119–22, December 2001.

[5] S. V. Bandara, S. D. Gunapala, D. Z-Y. Ting, S. B. Rafol, and J. K. Liu. Gaas/algaas multi-quantum-well based far infrared detectors for astronomy application. In *Proceedings of the Far-IR, Sub-mm & MM Detector Technology Workshop, April 1-3 2002, Monterey CA* [1]. In press.

[6] E. Batke, J. Kaminsky, J.P. Kotthaus, and J. Spector. Tunable far-infrared photovoltaic response in semiconductor field-effect devices. *Applied Physics Letters*, 54(2):131–3, January 1989.

[7] J.J. Bock, D. Chen, and A. E. Lange. A novel bolometer for infrared and

millimeter-wave astrophysics. *Space Science Reviews*, 74(1-2):229–35, October 1995.

[8] C. Cates, J. B. Williams, M. S. Sherwin, K. D. Maranowski, and A. C. Gossard. Tunable antenna-coupled intersubband terahertz (tacit) detectors for operation above 4k. In *Proceedings of the Eleventh International Symposium on Sapce Terahertz Technology, May 1-3, 2000, Ann Arbor, MI*, pages 389–96, 2000.

[9] G. Chattopadhyay, D. Miller, H.G. LeDuc, and J. Zmuidzinas. A dual-polarized quasi-optical sis mixer at 550 ghz. *IEEE Transactions on Microwave Theory and Techniques*, 48(10):1680–6, October 2000.

[10] T. W. Crowe, J. L. Hesler, R. M. Weikle, and S. H. Jones. Gaas devices and circuits for terahertz applications. *Infrared Physics & Technology*, 40(3):175–89, June 1999.

[11] John H. Davies. *The Physics of Low-Dimensional Semiconductors*, page 360. Cambridge University Press, New York, 1998.

[12] M. I. Dyakonov and M. S. Shur. Plasma wave electronics: terahertz detectors and sources using two dimensional electronic fluid in high electron mobility transistors. In *1997 Advanced Workshop on Frontiers in Electronics, WOFE '97 Proceedings (Cat. No.97TH8292)*, pages 105–8. IEEE, 1997.

[13] Bryan Galdrikian. *Nonlinear and Nonperturbative Dynamics in Quantum Wells*. PhD thesis, University of California Santa Barbara, August 1994.

[14] Supriya Goyal, Jordana Bandaruab, Jeffrey W. Beeman, and Eugene E. Haller. Germanium blocked impurity band detectors. In *Proceedings of the Far-IR, Sub-mm & MM Detector Technology Workshop, April 1-3 2002, Monterey CA* [1]. In press.

[15] D. Grischkowsky, S. Keiding, M. van Exter, and C. Fattinger. Far-infrared time-domain spectroscopy with terahertz beams of dielectrics and semiconduc-

tors. *Journal of the Optical Society of America B-Optical Physics*, 7(10):2006–15, October 1990.

[16] S.D. Gunapala, S.V. Bandara, J.K. Liu, E.M. Luong, S.B. Rafol, J.M. Mumolo, D.Z. Ting, J.J. Bock, M.E. Ressler, M.W. Werner, P.D. LeVan, R. Chehayeb, C.A. Kukkonen, M. Levy, P. LeVan, and M.A. Fauci. Quantum well infrared photodetector research and development at jet propulsion laboratory. *Infrared Physics & Technology*, 42(3–5):267–82, June 2001.

[17] J.N. Heyman, K. Unterrainer, K. Craig, B. Galdrikian, M.S. Sherwin, K. Campman, P.F. Hopkins, and A.C. Gossard. Temperature and intensity dependence of intersubband relaxation rates from photovoltage and absorption. *Physical Review Letters*, 74(14):2682–5, April 1995.

[18] H. Huebers, J. Schubert, A. Semenov, G.N. Gol'tsman, B.M. Voronov, E.M. Gershenzon, and G.W. Schwaab. Nbn phonon-cooled hot-electron bolometer as a mixer for thz heterodyne receivers. *Proceedings of the SPIE - The International Society for Optical*, 3828:410–16, 1999.

[19] B. S. Karasik, W. R. McGrath, M. E. Gershenson, and A. .v Sergeev. Photon-noise-limited direct detector based on disorder-controlled electron heating. *Journal of Applied Physics*, 87(10):7586–8, May 2000.

[20] Boris S. Karasik, Bertrand Delaet, William R. McGrath, Henry G. LeDuc, Jian Wei, Michael E. Gershenson, and Andrew V. Sergeev. Submm wave superconducting hot-electron direct detectors. In *Proceedings of the Far-IR, Sub-mm & MM Detector Technology Workshop, April 1-3 2002, Monterey CA*, 2002. In press.

[21] B.S. Karasik, A. Skalare, R.A. Wyss, W.R. McGrath, B. Bumble, B. LeDuc, J.B. Barner, and A.W. Kleinsasser. Low-noise and wideband hot-electron su-

perconductive mixers for thz frequencies. *1998 IEEE Sixth International Conference on Terahertz Electronics*, pages 1–4, 1998.

[22] J. Kawamura, C.-Y.E. Tong, R. Blundell, D.C. Papa, T.R. Hunter, F. Patt, G. Gol'tsman, and E. Gershenzon. Terahertz-frequency waveguide nbn hot-electron bolometer mixer. *IEEE Transactions on Applied Superconductivity*, 11(1):952–4, March 2001.

[23] A. R. Kerr, M. J. Feldman, and S.-K. Pan. Mma memo 161 - receiver noise temperature, the quantum noise limit, and the role of the zero-point fluctuations. In *Proceedings of the Eighth International Symposium on Space Terahertz Technology, March 25-27, 1997*, pages 101–111, 1997.

[24] R. Kohler, A. Tredicucci, F. Beltram, H. E. Beere, E. H. Linfield, A. G. Davies, D. A. Ritchie, and F Iotti, R. C. Rossi. Terahertz semiconductor-heterostructure laser. *Nature*, 417:156–159, May 9 2002.

[25] S. Komiyama, O. Astafiev, V. Antonov, T. Kutsuwa, and H. Hirai. A single-photon detector in the far-infrared range. *Nature*, 403(6768):405–7, January 2000.

[26] J.W. Kooi, J. Kawamura, J. Chen, G. Chattopadhyay, J.R. Pardo, J. Zmuidzinas, T.G. Phillips, B. Bumble, J. Stern, and H.G. LeDuc. A low noise nbtin-based 850 ghz sis receiver for the caltech submillimeter observatory. *International Journal of Infrared and Millimeter Waves*, 21(9):1357–73, September 2000.

[27] M. Kroug, Cherednichenko S., H. Merkel, E. Kollberg, B. Voronov, G. Gol'tsman, H.W. Huebers, and H. Richter. Nbn hot electron bolometric mixers for terahertz receivers. *IEEE Transactions on Applied Superconductivity*, 11(1):962–5, March 2001.

[28] Jung-Won Lee, Seog-Tae Han, Do-Young Byun, Bon-Chul Koo, and Yong-Sun Park. Development of srao 3 mm sis receiver. *International Journal of Infrared and Millimeter Waves*, 23(1):47–59, January 2002.

[29] Mark Lee, L.N. Pfeiffer, K.W. West, and K.W. Baldwin. Wide bandwidth millimeter wave mixer using a diffusion cooled two-dimensional electron gas. *Applied Physics Letters*, 78(19):2888–90, May 2001.

[30] W. R. McGrath, 2000. Private communication.

[31] W.R. McGrath, B.S. Karasik, A. Skalare, R. Wyss, B. Bumble, and H.G. LeDuc. Hot-electron superconductive mixers for thz frequencies. *Proceedings of the SPIE - The International Society for Optical Engineering*, 3617:80–8, 1999.

[32] P. Muralt. Micromachined infrared detectors based on pyroelectric thin films. *Reports on Progress in Physics*, 64(10):1339–88, October 2001.

[33] B.N. Murdin, W. Heiss, C.J.G.M. Langerak, S.-C. Lee, I. Galbraith, G. Strasser, E. Gornik, M. Helm, and C.R. Pidgeon. Direct observation of the lo phonon bottleneck in wide gaas/al/sub x/ga/sub 1-x/as quantum wells. *Physical Review B (Condensed Matter)*, 55(8):5171–6, February 1997.

[34] X.G. Peralta, S. J. Allen, M. C. Wanke, N. E. Harff, J. A. Simmons, M. P. Lilly, J. L. Reno, W. E. Baca, P. J. Burke, and J. P. Eisenstein. Resonant terahertz photoconductance of grating gated double quantum well field effect transistors. In *Proceedings of the Far-IR, Sub-mm & MM Detector Technology Workshop, April 1-3 2002, Monterey CA*, 2002. In press.

[35] A.G.U. Perera, S.G. Matsik, H.C. Liu, M. Gao, M. Buchanan, W.J. Schaff, and W. Yeo. 35 mu m cutoff bound-to-quasibound and bound-to-continuum ingaas qwips. *Infrared Physics & Technology*, 42(3–5):157–62, June 2001.

[36] A.G.U. Perera, W.Z. Shen, H.C. Liu, M. Buchanan, and W.J. Schaff. Gaas homojunction interfacial workfunction internal photoemission (hiwip) far-infrared detectors. *Materials Science & Engineering B (Solid-State Materials for Advanced*, b74(1–3):56–60, May 2000.

[37] M.B. Reine. Hgcdte photodiodes for ir detection: a review. *Proceedings of the SPIE - The International Society for Optical Engineering*, 4288:266–77, 2001.

[38] Dirk Rosenthal, Jeff W. Beeman, Norbert Geis, Ullrich Grözinger, Rainer Hönle, Reinhard O. Katterloher, Stefan Kraft, Leslie W. Looney, Albrecht Poglitsch, Walfried Raab, and Hilmar Richterd. Stressed ge:ga detector arrays for pacs and fifi ls. In *Proceedings of the Far-IR, Sub-mm & MM Detector Technology Workshop, 1-3 April 2002, Monterey CA* [1]. In press.

[39] D. Setiadi, Z. He, J. Hajto, and T.D. Binnie. Application of a conductive polymer to self-absorbing ferroelectric polymer pyroelectric sensors. *Infrared Physics & Technology*, 40(4):267–78, August 1999.

[40] M. S. Sherwin, C. Cates, B. Serapiglia, Y. Dora, J. B. Williams, K. Maranowski, A. C. Gossard, and W. R. McGrath. Tunable antenna-coupled intersubband terahertz (tacit) mixers: The quantum limit without the quantum liquid. In *Proceedings of the Far-IR, Sub-mm & MM Detector Technology Workshop, April 1-3 2002, Monterey CA*, 2002. In press.

[41] P. H. Siegel. Terahertz technology. *IEEE Transactions on Microwave Theory & Techniques*, 50(3):910–28, March 2002.

[42] F. Thiele, E. Batke, V. Dolgopolov, J.P. Kotthaus, G. Weimann, and W. Schlapp. Cyclotron-resonance-induced photovoltage of inversion electrons on gaas. *Physical Review B (Condensed Matter)*, 40(2):1414–17, July 1989.

[43] R. Tucker and M.J. Feldman. Quantum detection at millimeter wavelengths. *Reviews of Modern Physics*, 57(4):1055–113, October 1985.

[44] A. D. Turner, J. J. Bock, J. W. Beeman, J. Glenn, P. C. Hargrove, V. V. Hristov, H. T. Nguyen, S. Sethuraman, and A. L. Woodcraft. Silicon nitride micromesh bolometer array for submillimeter astrophysics. *Applied Optics*, 40(28):4921–32, October 2001.

[45] Mike Wanke. Thomas keating instructions : How to calibrate other detectors. Internal Manual, 1988.

[46] R.G. Wheeler and R.W. Ralston. Continuously voltage-tunable line absorption in surface quantization. *Physical Review Letters*, 27(14):925–8, October 1971.

[47] Jon Brett Williams. *Dissipation of THz frequency intersubband plasmons in quantum wells*. PhD thesis, University of California Santa Barbara, December 2000.

[48] Ralph E. Williams. *Modern GaAs processing methods*, page 115. Artech House, Boston, 1990.

[49] J.-X. Yang, F. Agahi, D. Dai, C.F. Musante, W. Grammer, K.M. Lau, and K.S. Yngvesson. Wide-bandwidth electron bolometric mixers: a 2deg prototype and potential for low-noise thz receivers. *IEEE Transactions on Microwave Theory and Techniques*, 41(4):581–9, April 1993.

[50] K.S. Yngvesson. Ultrafast two-dimensional electron gas detector and mixer for terahertz radiation. *Applied Physics Letters*, 76(6):777–9, February 2000.

[51] K.S. Yngvesson, E. Gerecht, C.F. Musante, Y. Zhuang, M. Ji, T.M. Goyette, J. Dickinson, J. Waldman, P.A. Yagoubov, G.N. Gol'tsman, B.M. Voronov, and E.M. Gershenzon. Low-noise heb heterodyne receivers and focal plane arrays for the thz regime using nbn. *Proceedings of the SPIE - The International Society for Optical Engineering*, 3795:357–68, 1999.

Appendix A

Intensity Calibration

The THz intensity must be calibrated in order to quantify the power incident on or absorbed by the detector in an absolute, rather than relative, way. The calibration procedure used here followed the method outlined in Mike Wanke's instructions pamphlet[45] and used the Thomas Keating to calibrate the reference detector used in the optical measurements. This information, along with the transmission of several materials and geometric calculations allow the intensity to be calibrated.

A.1 Measurements

The Thomas Keating is an energy detector that can be calibrated absolutely. It is comprised of a NiCr film in a sealed cavity with TPX windows. A microphone detects the acoustic vibrations generated when the NiCr film absorbs incident THz light and heats up the air around it. The output signal is proportional to the energy deposited in the NiCr film. The NiCr film is impedance-matched to air, so half the incident power gets absorbed in the film. The energy incident on the Thomas-Keating can be expressed,

$$\text{Energy}_{inc} = \frac{2(\text{Energy Absorbed})}{(\text{TPX Transmission})} \tag{A.1.1}$$

The output signal of the Thomas Keating can be calibrated by applying voltage pulses to the NiCr film, causing Joule heating. The Thomas-Keating calibration recently done by Xomalin Peralta was used for these calculations.

The Thomas Keating detector was used to calibrate the reference detector to the THz energy at the position of the sample. The THz optical setup, shown in Figure 5.4, splits the incident THz beam with a beamsplitter, diverting part of it to be focused on a reference pyroelectric detector, with the remainder focused into the cryostat. For the calibration of the reference detector, the cryostat was removed, and the Thomas Keating was put in its place, as shown in Figure A.1. Because the NiCr foil is susceptible to damage, the Thomas Keating was put beyond the focal point of the off-axis parabolic mirror. It was placed at a distance that allowed the beam to spread out and cover as much of the TPX window as possible without clipping any of the beam. The Thomas Keating was placed at Brewster's angle with respect to the optical axis of the parabolic mirrors to minimize the reflection losses at the TPX window. The THz beam was diverging, as the detector was beyond the focal point, so the outer portions of the beam were not exactly at Brewster's angle and had a small reflection loss. This loss is small, and is included in the error estimate for the Thomas Keating measurement. Simultaneous measurements from the reference pyroelectric detector and the Thomas Keating, averaged over the same set of FEL pulses, were taken over a range of attenuation between where the Thomas Keating barely registered a signal to where the reference detector saturated. The attenuation was effected by placing 10-mil mylar attenuators, with their optical axes aligned, right by the FEL port, in front of the beam splitter. With these measurements, the reference detector's signal was calibrated to the total energy in the FEL beam.

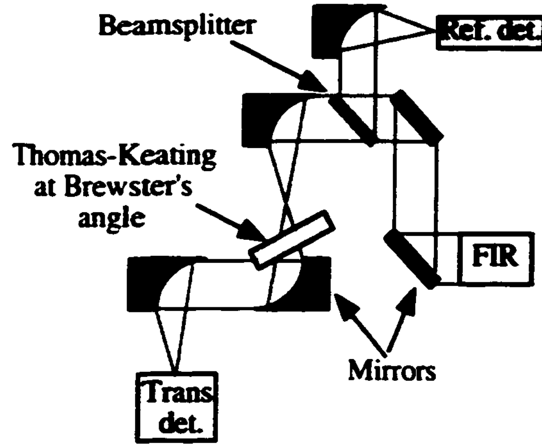

Figure A.1: Optical setup showing placement of Thomas-Keating detector for calibration of reference pyroelectric detector. The Thomas-Keating was placed at Brewster's angle, behind the focus of the off-axis parabolic mirrors.

A.2 Transmission Factors

The power inside the device can be expressed as a product of the energy outside the sample and several transmission factors.

$$\mathrm{Power}_{\mathrm{in\ sample}} = \left[\frac{2(\mathrm{Energy}_{TK})}{(T_{TPX})(W_{\mathrm{THz\ pulse}})}\right] T_{\mathrm{polyethylene}} T_{\mathrm{cryostat}} T_{\mathrm{GaAs/He\ gas}} \mathrm{G} \tag{A.2.1}$$

The power of the beam at the plane of the sample is the energy measured on the reference detector, converted by the calibration into the energy in the FEL beam, divided by the pulse width of the FEL pulses, $W_{\mathrm{THz\ pulse}}$, and multiplied by the transmission percentages of the black polyethylene optical filter, $T_{\mathrm{polyethylene}}$, and the two polypropylene cryostat windows in the beam path, T_{cryostat}. The power inside the device is the product of the power at the plane of the sample inside the helium flow cryostat, the transmission of the GaAs-He gas interface, $T_{\mathrm{GaAs/He\ gas}}$, and the geometrical factor, G, of the overlap of the Gaussian power distribution in the incident beam and the rectangular window around the active region. Table A.2 lists the values and relative errors for these parameters.

This window was formed of pieces of aluminum foil, to only allow illumination

Parameter	Value	Uncertainty
T_{TPX}	0.54	4%
$W_{\text{THz pulse}}$	3.7μs	7%
$T_{\text{cryostat}}T_{\text{polyethylene}}$	0.42	10%
$T_{\text{GaAs/He gas}}$	0.68	+0% -2%
G	0.476	+5% -13%
E_{TK}		10%

Table A.1: Parameters used in the intensity calculations, with the uncertainty attributable to each

of the area of the device under the front gate and to keep light from hitting the ohmic contacts of the source and drain or from leaking around the outside of the sample. Waveguide effects are ignored in the calculation of the power inside the sample. The intensity of the Gaussian beam is approximately uniform in the growth direction of the sample, dropping only 2% below maximum at the edges of the sample window. The THz fields in the sample can be approximated as being in the TEM mode of a parallel-plate waveguide filled with dielectric. In the plane of the sample, the window was much larger than the full width at half-maximum (FWHM) of the incident THz beam, so in that direction, the THz fields are only confined by the dielectric. The geometric factor G is the ratio of the power of the portion of the beam subtended by the window to the total power in the beam.

The transmission of TPX at 103cm^{-1}was taken from a graph with data attributed to M. Urban in Mike Wanke's Thomas-Keating instructions[45].

The FEL pulse width was taken from traces of FEL pulses taken with a fast detector by Tom King. The width was taken as the time between when the power rose and fell through a point half of the maximum power, a sort of full-width-half-maximum. The recorded pulses were for the frequency $84cm^{-1}$, but the pulse shape should be very similar for the frequency I used in these measurements, $103cm^{-1}$, since the two frequencies both come from the same FEL beamline and have similar gain characteristics.

The transmission factors for the polyethylene optical filter and polypropylene

film used in the cryostat windows were measured by Fourier Transform Infrared (FTIR) spectroscopy. The entire cryostat was put in the FTIR transmission path, so the transmission through both the entering and exiting sets of windows and filters was measured. The square root of that transmission is used here, for the transmission through only one set of windows, to get the power inside the cryostat.

The transmission of the GaAs/He gas interface was calculated from simple theory, with a value of the GaAs index of refraction for the far-infrared of 3.6[15]. The uncertainty from the theory is negligible, and the error in the transmission is because normal incidence was calculated, although the THz beam in this case was converging. Most of the beam will be contained within 16°, the approximate incident angle of a portion of the THz beam just hitting the far edge of the focusing off-axis parabolic mirror. The portion of the beam just hitting the near edge of the parabolic mirror will have a large incident angle on the sample, but in the Gaussian distribution, most of the power of the THz beam will be in the center angles, at much smaller angles.

The value of G, the ratio of the power of the portion of the beam subtended by the window to the total power in the beam, was determined by calculating the ratio of appropriate integrals over the Guassian distribution. The full width at half-maximum (FWHM) for the THz beam were measured by scanning a small aperture on the sample holder through the beam in the horizontal and vertical directions, centered on the peak THz power. The uncertainty in G is comprised of two parts, from an estimate in the uncertainty from the measurements of the FWHM of the beam and size of the window opening on the sample, and from the effects of possible misalignment of the sample with the THz beam center. The effects of possible misalignment from the center, peak power of the THz beam would only reduce the power transmitted to the sample, making the negative error bound larger than the positive error bound. In the plane of the quantum well, the window is larger than the beam FWHM, so misalignment is irrelevant, and only the misalignment in the growth direction of the well contributes to the error bound.

$\frac{\Delta Power_{outside}}{Power_{outside}}$	$\pm$ 16%
$\frac{\Delta Power_{incident}}{Power_{incident}}$	+17% −21%
$\frac{\Delta Power_{inside}}{Power_{inside}}$	+17% −21%

Table A.2: The relative errors in the calibrations of several powers used in device calculations.

A.3 Error Bounds

Since all the sources of uncertainty and error in determining the intensity are independent, the total error is the square root of the sum of the squares of the relative errors,

$$\frac{\Delta I}{I} = \sqrt{\sum \left(\frac{\Delta N}{N}\right)^2} \tag{A.3.1}$$

The total uncertainty in the calibration for several powers used in the calculations are listed in Table A.3. $Power_{outside}$ is the power in the full beam outside of the sample, but inside the cryostat. $Power_{incident}$ is the power in the portion of the beam that passed through the aluminum foil aperture to hit the sample face. $Power_{inside}$ is the power just inside the front face of the sample, taking into account the GaAs/He gas interface, but ignoring any effects of waveguide modes. The relative error for calibrating intensities is taken from the appropriate power value.

Appendix B

Calculating the Electric Field and Charge Density

The electrostatic environment at the channel quantum well can be described by the front and back gate voltages, or equivalently by the static electric field and the charge density in the well. The field and charge density can be changed independently by moving the gate voltages appropriately. Moving the gate voltages in opposite directions varies the static electric field, and moving them together with respect to the potential at the well changes the charge density.

B.1 Electric Field

When the channel quantum well contains charge, then there is a discontinuity in electric across the well, and the static electric field at the well is taken to be the average. Following Jon Williams' dissertation, Ref.[47], the electric field can be expressed,

$$E_{QW} = \frac{V_{fg}}{2d_{fg}} - \frac{V_{bg}}{2d_{bg}} \tag{B.1.1}$$

where V_{fg} and V_{bg} are the front and back gate voltages with respect to the potential at the channel quantum well, and d_{fg} (d_{bg}) is the distance between the channel and

front (back) gate. The polarity of this equation is that negative fields tend to push electrons towards the back gate, and positive fields push electrons towards the front gate at the surface of the wafer. Equation B.1.1 ignores band-bending effects and any built-in field, and approximating the quantum well as being infinitessimally thin. The built-in electric field comes from asymmetric ionized dopant concentrations on either side of the well and subsequent band bending. The charge asymmetry can be the result of slight differences in doping profiles during growth or in small differences in dopant ionization during sample cooldown.

In the case where the quantum well contains no mobile charge or the well is electrically isolated so no charge can flow into or out of the well, then the electric field is constant between the front and back gates, and the static electric field is given by,

$$E_{QW} = \frac{V_{fg} - V_{bg}}{d_{fg} + d_{bg}} \tag{B.1.2}$$

Most of the data discussed in this work, however, is for the case where the channel quantum well does contain mobile charge and is connected to an outside circuit. So, unless otherwise specified, the average electric field given in Equation B.1.1 will be used.

B.2 Charge Density

The charge density in the well was determined by integrating the capacitance from depletion to the gate voltages of interest. As the capacitance was determined by measuring the AC current, the measurement was only sensitive to the mobile charge. The non-mobile charge was caught in traps and could not contribute to the measured current. The charge density was integrated using Jon Williams' LabView VI in the CV library. This VI uses the first several points, all in the depletion regime, to fit and subtract off a baseline capacitance, to get rid of background capacitances from cables in the circuit and the like.

The capacitance was measured by holding the back gate voltage fixed and sweeping the front gate voltage. The gate voltages over which the capacitance and charge density could be determined directly differ from those used in the photosignal scans. In order to determine the values of the charge density at the gate voltages where the photosignal and other data were collected, the charge density data was interpolated. Matlab's piecewise bilinear algorithm was used for the interpolation to get a moderately smooth distribution of the interpolated values without introducing values outside the range of nearby data points.

The bilinear interpolation algorithm calculates the interpolated value as a linear combination of the four nearest surrounding points. Thus, the algorithm cannot generate an interpolated value for gate voltage points outside the range of front and back gate voltages for which the capacitance was measured. In particular, the lowest back gate voltage for which the capacitance was measured was 0V, but photosignal data was taken at lower back gate voltages. In order to accommodate this range of gate voltage parameter space, charge densities for $V_{bg} = -0.5V$ were extrapolated from the measured charge densities. The measured charge densities varied gradually with both gate voltages and were used to create a moderately-fine evenly-spaced mesh of interpolated values. Slices of this mesh, taken at constant front gate voltage, were fit with a piecewise polynomial spline, which was then used to extrapolate a charge density value for $V_{bg} = -0.5V$ at each front gate voltage in the mesh. The set of extrapolated values was concatenated with measured data to make an augmented data set, which was used for the actual interpolation of the charge densities to the gate voltages where the photosignal data was taken. By augmenting the data set, most of the interpolations used actual data, and only the voltage points for which interpolation was otherwise not possible used the extrapolated values in interpolation. In the few remaining gate voltage points that still could not be interpolated using the bilinear algorithm, the value of the nearest neighbor point was simply copied.

The different levels of calculation in the interpolation of the charge density yields varied levels of potential error across the range of gate voltages interpolated. How-

ever, the charge density data was relatively smoothly varying, so the extrapolation methods used here are not expected to add significantly to the error in the final values.